Powder Technology 468 (2026) 121670

Contents lists available at ScienceDirect

Powder Technology

journal homepage: www.journals.elsevier.com/powder-technology

Molerus and Wirth's heat transfer model for bubbling fluidized beds: Proposal for an extended model including immersed tube banks and particle cross-flow

Stefan Thanheiser

Institute for Energy Systems and Thermodynamics, TU Wien, Getreidemarkt 9/E302, 1060 Wien, Austria

HIGHLIGHTS

- Molerus and Wirth's model was extended with new dimensionless numbers.
- Heat transfer data was collected from experiments and secondary sources.
- The extended heat transfer model accounts for tube diameter and tube packing density.
- Relevant conditions for a significant impact of particle cross-flow were identified.

GRAPHICAL ABSTRACT

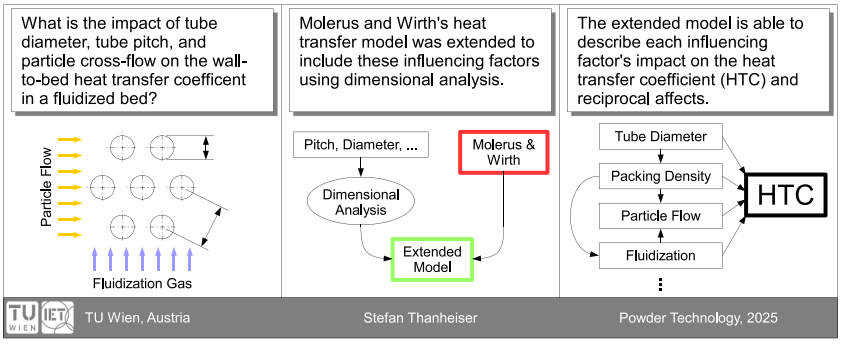

ARTICLE INFO

Keywords:
Fluidized bed heat exchanger
Tube bundle
Contact time
Pitch
Lateral mixing
Thermal energy storage

ABSTRACT

While there are many semi-empirical correlations for estimating the wall-to-bed heat transfer coefficient in a fluidized bed, most are only usable in a limited range of operating conditions. The correlation developed by Molerus and Wirth (1997) provides the most expansive and successful model; however, it does not consider the influence of the properties of an immersed tube bank or a horizontal movement of particles (cross-flow). This study expands Molerus and Wirth's correlation to include these additional influencing factors by identifying and introducing new dimensionless factors using dimensional analysis. Collected secondary data and measurements from a test rig were used to evaluate the extended model. The model's estimates largely align with the collected secondary data and previously published models describing the influence of tube diameter and tube packing density on the wall-to-bed heat transfer coefficient. The model also provides new insight into the conditions under which a particle cross-flow contributes significantly to the wall-to-bed heat transfer coefficient. Future research should use these findings to conduct targeted measurements and further improve the model's predictions.

E-mail address: stefan.thanheiser@tuwien.ac.at.

https://doi.org/10.1016/j.powtec.2025.121670
Received 10 June 2025; Received in revised form 5 August 2025; Accepted 19 September 2025
Available online 21 September 2025

Nomenclature

Abbreviations

FBHE	Fluidized bed heat exchanger
HTC	Heat transfer coefficient
HTF	Heat transfer fluid
RMSE	Root mean square error
SiO_2	Silicon dioxide
sCO_2	Supercritical carbon dioxide
TES	Thermal energy storage

Symbol

A	Heat transfer area or cross-section, m^2
$A…D$	Submatrix, –
Ar	Archimedes number, –
C	Cross-flow constant, –
c	Isobaric specific heat capacity, J/kgK
d	Diameter, m
$d(\pi_5)$	Damping function, –
G	Gas convection constant, –
g	Gravitational acceleration, m/s^2
H_0	Null hypothesis, –
H_1	Extended model, –
h	Heat transfer coefficient, W/m^2K
k	Thermal conductivity, W/mK
l_{lam}	Laminar length scale, m
$\dot{m}$	Mass flow, kg/s
Nu	Nusselt number, –
P	Particle convection constant, –
P_{el}	Electric power, W
Pe	Peclet number, –
p	Pressure (Pa) or tube pitch (m)
$p(\pi_9)$	Packing density function, –
R^2_{adj}	Adjusted coefficient of determination, –
$r(\pi_{10})$	Horizontal particle transport resistance, –
r_{total}	Total particle transport resistance, –
s	Tube spacing
$s(\pi_8)$	Size function, –
T	Temperature, K
$t(\pi_5)$	Turbulence function, –
w	Velocity, without subscript: fluidization velocity, m/s
ε	Mean bed voidage, –
μ	Dynamic viscosity, Pa s
π	Dimensionless variable, –
ρ	Density, kg/m^3
φ_S	Particle sphericity, –
ψ	Tube bank void fraction, –

Subscripts

bed	Fluidized bed
cf	Cross-flow
diag	Diagonal
e	Excess
g	Fluidization gas
gc	Gas convection
h	Horizontal
lam	Laminar
max	Maximum
mf	Minimum fluidization
min	Minimum
p	Particle
pc	Particle convection
t	Tube
tb	Tube bank
turb	Turbulent
single	Single tube
surf	Surface
v	Vertical
1…10	Index

1. Introduction

1.1. Background

Fluidized beds are widely used for their very good heat transfer properties [1] (p. 291), such as drying [2], catalytic cracking [3], and waste heat recovery [4] (pp. 12–13). Some thermal energy storage (TES) systems utilize a particle cross-flow – a horizontal movement of particles [5] (p. 245) – and an immersed heat exchanger to create counter-current heat exchangers [6] (p. 1). Design and optimization of this type of fluidized bed heat exchanger (FBHE) requires detailed knowledge of the heat transfer coefficient (HTC) between the tubes' outer wall and the surrounding fluidized bed [6] (p. 1).

1.2. Previous research

Models describing the wall-to-bed HTC can be divided into two categories. The first category is *mechanistic models*, which aim to describe the process by which particles exchange thermal energy with a surface immersed in the fluidized bed [1] (pp. 294–295). These include the "packet theory" by Mickley and Fairbanks [7] as well as models assuming unsteady thermal conduction between the heat transfer surface and particles (see Botterill et al. [8]) or between layers of fluidization gas and particles (see Gabor [9]). Using these models to predict the wall-to-bed HTC is often not feasible [10] (p. 190) since they usually require knowledge of physical data not readily available to the user [11] (p. 92).

The second category comprises *(semi-) empirical correlations*, which aim to predict the wall-to-bed HTC under different operating conditions [1] (pp. 302–303). Some of the more widely used models include Martin [12], Andeen and Glicksman [13], Borodulya [14], Bao [15], Grewal [16], Grewal and Saxena [17], and Molerus and Wirth [18]. These models take different influencing factors on the wall-to-bed HTC into account, their predictions do not agree with each other [19] (p. 505), and they cannot be reasonably extrapolated beyond the (usually very narrow) conditions for which they have been developed [1] (p. 303). Only the correlation developed by Molerus and Wirth [18] covers a wide range of operating conditions, and it has therefore been described as the "most successful" correlation [1] (p. 303).

1.3. Research problem

This study focuses on FBHEs that employ a particle cross-flow and an immersed heat exchanger consisting of a staggered array of horizontal tubes. Previous research has demonstrated that larger tube diameters [20] (p. 162) and a denser tube arrangement [21] (pp. 368–369) lead to lower wall-to-bed HTCs. However, while successful, Molerus and Wirth's correlation for the wall-to-bed HTC does not consider the tube diameter or the heat exchanger tubes' packing density as direct influencing factors [22] (pp. 69–70). Additionally, observations made by the authors suggest a significant impact of particle cross-flow on the wall-to-bed HTC, which is also not taken into account by Molerus and Wirth's correlation [22] (pp. 69–70).

1.4. Research objectives

This study aims to extend Molerus and Wirth's correlation to include the influence of the diameter and packing density of the heat exchanger tubes as well as the impact of particle cross-flow on the wall-to-bed HTC. The proposed model is evaluated against Molerus and Wirth's original model, which is the null hypothesis in this study.

1.5. Outline

Section 2 covers the development of the proposed model and the methods used to evaluate it. Section 2 includes a detailed description of Molerus and Wirth's original model in Section 2.2 that serves as this study's theoretical framework. The results of the model's evaluation are described in Section 3, and the results are interpreted and discussed in Section 4.

All data collected in this study is available in the data repository [23]. Software for data analysis is available in the software repository [24].

2. Methods

To include the influences of tube diameter, tube packing density, and particle cross-flow in Molerus and Wirth's correlation for the wall-to-bed HTC, the following steps were taken.

- Molerus and Wirth identified a list of influencing factors of wall-to-bed heat transfer and used dimensional analysis to derive dimensionless factors that constitute the building blocks of their correlation [25] (pp. 37–38). Therefore, Molerus and Wirth's original list of influencing factors was extended to include tube diameter, tube packing density, and the intensity of the particle cross-flow, and a new set of dimensionless factors was derived using dimensional analysis (Section 2.1).
- The functional structure of Molerus and Wirth's correlation was analyzed in detail to enable subsequent modifications (Section 2.2).
- Molerus and Wirth's correlation was extended by the previously identified new dimensionless factors for tube diameter, tube packing density, and the particle cross-flow (Section 2.3) to create the new model (hereafter the "extended model").
- Secondary data (i.e., data from previously published literature) was collected of wall-to-bed heat transfer measurements using different tube diameters and tube packing densities (Section 2.4).
- A test rig able to introduce a specified particle cross-flow into a fluidized bed containing a staggered array of horizontal tubes was used to measure the impact of particle cross-flow on the wall-to-bed HTC (Section 2.5).
- Both the collected secondary data and the measurements from the test rig were used to evaluate the extended model and compare it to the null hypothesis (Section 2.6).

2.1. Dimensional analysis

Following Molerus and Wirth [22] (pp. 69–70), dimensionless factors were derived from a set of significant influencing factors of wall-to-bed heat transfer using dimensional analysis. For this purpose, Molerus and Wirth's original list of influencing factors was extended by additional factors to account for the influence of the heat exchanger's tube diameter, tube packing density, and particle cross-flow. Fig. 1 depicts the characteristic parameters for quantifying tube packing density and particle cross-flow. [26]

Some authors, such as Lechner et al. [26] (p. 17), have used several of the pitch definitions in Fig. 1 simultaneously to characterize tube packing density and its influence on the wall-to-bed HTC. However, other authors, such as Saxena [27] (p. 155), have only found the horizontal tube pitch p_h to have a significant impact on the wall-to-bed HTC. To avoid unnecessary complexity, only the horizontal tube pitch p_h was used in this study to account for the impact of the tube bank's packing density on the wall-to-bed HTC.

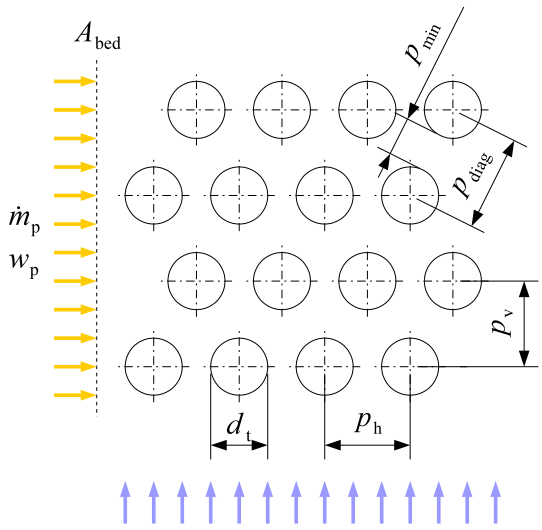

Fig. 1. Cross-section of a fluidized bed with a staggered array of horizontal tubes. Blue arrows (vertical) show flow of fluidization gas; orange arrows (horizontal) indicate particle flow. Tube pitch definitions [26] (p. 17): p_h horizontal pitch, p_v vertical pitch, p_{diag} diagonal pitch, p_{min} minimum pitch. Parameters: A_{bed} vertical cross-section of the fluidized bed, $\dot{m}_p$ particle mass flow, w_p mean horizontal particle velocity, d_t outside tube diameter.

The mean horizontal particle velocity w_p was chosen to characterize the intensity of the particle cross-flow and is defined as (see Fig. 1)

$$w_p = \frac{\dot{m}_p}{\rho_p (1 - \varepsilon_{mf}) A_{bed} \psi} \tag{1}$$

where ρ_p is the (raw) particle density, ε_{mf} is the bed voidage at minimum fluidization conditions, and ψ is the tube bank's void fraction (fraction of free space between tubes) defined as [28] (p. 726):

$$\psi = 1 - \frac{d_t}{8 p_v} \pi \text{ for } \frac{p_h}{2 d_t} \geq 1 \tag{2}$$

Table 1 presents the original list of influencing factors identified by Molerus and Wirth [22] (pp. 69–70) extended by the new influencing

Table 1
Influencing factors of wall-to-bed heat transfer.

Symbol	Description	Dimension
h	Heat transfer coefficient	W/m^{2}K
c_g	Specific heat capacity, fluidization gas	J/kgK
c_p	Specific heat capacity, particles	J/kgK
ρ_g	Fluidization gas density	kg/m^3
$\rho_p - \rho_g$	Difference between particle and fluidization gas density	kg/m^3
μ_g	Fluidization gas dynamic viscosity	Pa s
k_g	Fluidization gas thermal conductivity	W/mK
w_e	Excess fluidization velocity	m/s
w_{mf}	Minimum fluidization velocity	m/s
$1 - \varepsilon_{mf}$	Volume fraction of particles at minimum fluidization	–
g	Gravitational acceleration	m/s^2
d_t	Heat exchanger tube diameter	m
p_h	Horizontal tube pitch	m
w_p	Mean horizontal particle velocity	m/s

Those above the horizontal line are the original factors used by Molerus and Wirth [22] (pp. 69–70); Factors below the line were added. Definitions: $w_e = w - w_{mf}$, with w being the superficial fluidization velocity [29] (p. 79); ε_{mf} is bed voidage (volume fraction of gas) at minimum fluidization conditions [30] (p. 3).

factors tube diameter d_t (a focus of this study), horizontal pitch p_h, and mean horizontal particle velocity w_p.

The particle diameter d_p as an influencing factor of wall-to-bed heat transfer is replaced by the minimum fluidization velocity w_{mf} and the volume fraction of particles at minimum fluidization conditions $1-\varepsilon_{mf}$ in Molerus and Wirth's correlation [22] (p. 69). The Archimedes number Ar [29] (p. 69)

$$\mathrm{Ar} = \frac{d_p^3 \rho_g (\rho_p - \rho_g) g}{\mu_g^2} \tag{3}$$

can therefore not be defined using the variables in Table 1; hence, the Archimedes number is not a dimensionless factor in Molerus and Wirth's correlation. However, it is still relevant for the characterization of different flow conditions and heat transfer regimes in the fluidized bed described later (Section 2.2).

The definition of the mean horizontal particle velocity w_p in Eq. 1 uses the volume fraction of particles at minimum fluidization conditions $(1-\varepsilon_{mf})$ instead of at the actual conditions $(1-\varepsilon)$. This simplifies the equation by using a parameter that is both readily available to the user and already an influencing factor of wall-to-bed heat transfer (see Table 1). The dependence of bed voidage ε on the excess fluidization velocity w_e [31] (p. 155) and its impact on the wall-to-bed HTC is implicitly accounted for in the model developed in this study by including the excess fluidization velocity w_e as an influencing factor of wall-to-bed heat transfer. This also follows the approach by Molerus and Wirth.

Detailed bubble properties are not considered direct influencing factors of wall-to-bed heat transfer in Molerus and Wirth's model; see Table 1. Other authors, such as Mickley and Fairbanks [7] (p. 375), include the bubble frequency in their models. It is generally agreed that bubbles are the driver of (vertical) particle movement [32] (p. 144) and, thereby, particle convective heat transfer [33] (p. 11). However, bubble dynamics and wall-to-bed heat transfer in fluidized beds depend on the same physical properties of particles, fluidization gas, and excess fluidization velocity [11] (p. 95). Since all of these influencing factors are already included in Molerus and Wirth's model, both the original and the extended model implicitly account for bubble dynamics without introducing parameters that are often unavailable to the user.

The influencing factors from Table 1 were used to create the *dimensional set* [34] (p. 164) shown in Table 2.

The dimensional set in Table 2 was used to derive the new set of dimensionless factors. The submatrix D was modified slightly from the identity matrix to obtain dimensionless variables similar to those from Molerus and Wirth [22] (p. 70). Using the laminar flow length scale l_{lam} from Molerus and Wirth [25] (p. 40),

$$l_{lam} = \left(\frac{\mu_g}{\sqrt{g}\,(\rho_p - \rho_g)} \right)^{2/3} \tag{4}$$

and adding the factor 0.5 to π_2 (same as Molerus and Wirth [35], pp. 80–81) results in the dimensionless variables (pi-factors) in Table 3.

Factors $\pi_1 \ldots \pi_5$ and π_7 are identical to Molerus and Wirth's original dimensionless variables, whereas π_6 was modified to look similar to π_5 instead of the original definition of w_e/w_{mf} (which is now identical to π_5/π_6) [22] (p. 70).

Factor π_8 accounts for the impact of the tube diameter d_t on the wall-to-bed HTC by relating it to the laminar flow length scale l_{lam}. It can be interpreted as the relative contact time between particles and the heat transfer surface. Factor π_9 relates the tube diameter d_t to the horizontal pitch p_h, which is identical to the inverse horizontal spacing $1/s_h$ [26] (p. 17).

Factors π_5, π_6, and π_{10} all comprise a velocity w and the term $\left(\rho_p c_p / (k_g g)\right)^{1/3}$. This term relates the transport of particle heat capacity, represented by $(\rho_p c_p)^{1/3} w$, to the thermal conduction between the par-

Table 3
Dimensionless variables (pi-factors) derived from Table 2 and their descriptions.

Pi-factor	Description
$\pi_1 = \frac{h l_{lam}}{k_g}$	Nusselt number [36] (p. 64)
$\pi_2 = \frac{k_g}{2 c_p \mu_g}$	Particle transport resistance [25] (p. 42)
$\pi_3 = \frac{c_g \mu_g}{k_g}$	Prandtl number [22] (p. 70)
$\pi_4 = \frac{\rho_g}{\rho_p - \rho_g}$	Inverse relative particle weight minus buoyancy [25] (p. 38)
$\pi_5 = \left(\frac{\rho_p c_p}{k_g g}\right)^{1/3} w_e$	Dimensionless excess fluidization velocity [36] (p. 62)
$\pi_6 = \left(\frac{\rho_p c_p}{k_g g}\right)^{1/3} w_{mf}$	Dimensionless minimum fluidization velocity
$\pi_7 = 1 - \varepsilon_{mf}$	Volume fraction of particles [36] (p. 62)
$\pi_8 = \frac{d_t}{l_{lam}}$	Relative contact time
$\pi_9 = \frac{d_t}{p_h}$	Tube packing density
$\pi_{10} = \left(\frac{\rho_p c_p}{k_g g}\right)^{1/3} w_p$	Dimensionless mean horizontal particle velocity

Table 2
Dimensional set.

	h	c_p	c_g	ρ_g	w_e	w_{mf}	$1-\varepsilon_{mf}$	d_t	p_h	w_p	k_g	$\rho_p-\rho_g$	g	μ_g
m	0	2	2	−3	1	1	0	1	1	1	1	−3	1	−1
s	−3	−2	−2	0	−1	−1	0	0	0	−1	−3	0	−2	−1
kg	1	0	0	1	0	0	0	0	0	0	1	1	0	1
K	−1	−1	−1	0	0	0	0	0	0	0	−1	0	0	0
π_1	1	0	0	0	0	0	0	0	0	0	−1	−2/3	−1/3	2/3
π_2	0	−1	0	0	0	0	0	0	0	0	1	0	0	−1
π_3	0	0	1	0	0	0	0	0	0	0	−1	0	0	1
π_4	0	0	0	1	0	0	0	0	0	0	0	−1	0	0
π_5	0	1/3	0	0	1	0	0	0	0	0	−1/3	1/3	−1/3	0
π_6	0	1/3	0	0	0	1	0	0	0	0	−1/3	1/3	−1/3	0
π_7	0	0	0	0	0	0	1	0	0	0	0	0	0	0
π_8	0	0	0	0	0	0	0	1	0	0	0	2/3	1/3	−2/3
π_9	0	0	0	0	0	0	0	1	−1	0	0	0	0	0
π_{10}	0	1/3	0	0	0	0	0	0	0	1	−1/3	1/3	−1/3	0

This matrix consists of four submatrices separated by fine lines: A in the top right, B top left, $C = -D\left(A^{-1}B\right)^{\mathrm{T}}$ bottom right, and D bottom left [34] (p. 175). Submatrices A and B constitute the dimensional matrix, indicating the exponents of each dimension (row) for every influencing factor in Table 1 (column). Submatrices C and D include the exponents of every influencing factor contained in each dimensionless variable $\pi_1 \ldots \pi_{10}$.

ticles and the heat transfer surface through a layer of gas, represented by k_g [36] (p. 62).

2.2. Analyzing Molerus and Wirth's original correlation

This section describes Molerus and Wirth's original correlation for the wall-to-bed HTC to facilitate subsequent implementations of the new dimensionless variables derived in Section 2.1. The definitions of the dimensionless variables in Table 3 are used from this point on.

Molerus and Wirth defined a Nusselt number Nu as the sum of a particle convective Nusselt number $\mathrm{Nu_{pc}}$ and a gas convective Nusselt number $\mathrm{Nu_{gc}}$ [36] (pp. 55–56, 62, 64).

$$\mathrm{Nu} = \mathrm{Nu_{pc}} + \mathrm{Nu_{gc}} \tag{5}$$

The (total) Nusselt number Nu is identical to the first pi-factor [36] (p. 64).

$$\mathrm{Nu} = \pi_1 = \frac{h l_{\mathrm{lam}}}{k_g} \tag{6}$$

The particle convective Nusselt number $\mathrm{Nu_{pc}}$ characterizes the heat transfer between a surface and particles moving past them, in which the particles act as carriers of thermal energy [33] (p. 11). The gas convective Nusselt number $\mathrm{Nu_{gc}}$ encompasses the heat transfer between a surface and the passing fluidization gas [1] (p. 294). Both particle and gas convective heat transfer and the relative weight of each depend on the (dimensionless) excess fluidization velocity π_5 and the Archimedes number Ar [25] (pp. 36, 47). This is demonstrated in Fig. 2.

If the Archimedes number Ar is below 10^2, the fluidized bed is in the laminar flow regime and only particle convection contributes to heat transfer [25] (pp. 38, 45). On the other hand, if the Archimedes number Ar is greater than 10^5, the fluidized bed is in the turbulent flow regime and only gas convection plays a role [25] (pp. 44–45). In both cases, the Nusselt number asymptotically reaches its respective maximum value with increasing excess fluidization velocity [25] (pp. 45–47); see Fig. 2.

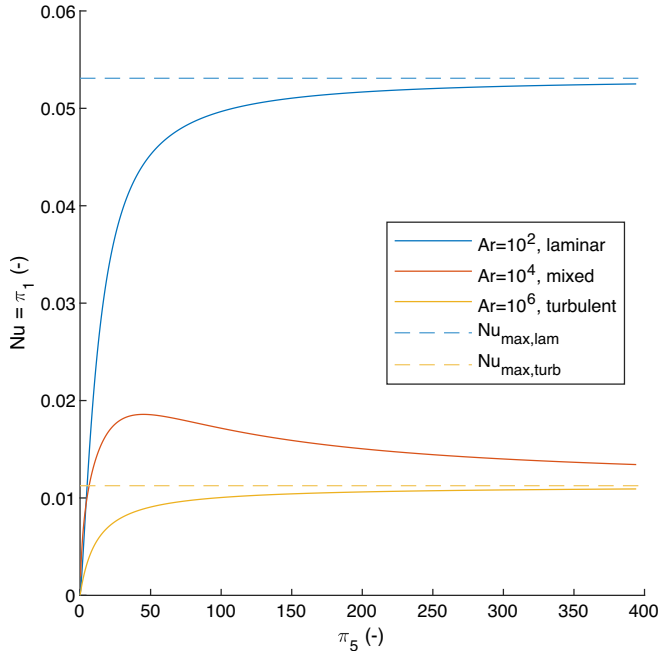

Fig. 2. Nusselt number $\mathrm{Nu} = \pi_1$ over dimensionless excess fluidization velocity π_5 according to the correlation by Molerus and Wirth [36] (p. 64). Conditions: Bed temperature $T = 20\,^{\circ}\mathrm{C}$, bed pressure $p = 0.1$ MPa. Particles: SiO_2, $\rho_p = 2648\ \mathrm{kg/m^3}$, $\varepsilon_{\mathrm{mf}} = 0.45$, sphericity $\varphi_S = 0.8$. Fluidization gas: dry air. Abbreviations: max = maximum, lam = laminar, turb = turbulent. The vertical order of legend entries is identical to their appearances in the graph.

If the Archimedes number Ar is between 10^2 and 10^5, the fluidized bed is in the mixed laminar/turbulent regime [25] (p. 47). In this case, the heat transfer gradually shifts from a more particle-convective (laminar) regime to the purely gas-convective (turbulent) regime with increasing excess fluidization velocity, asymptotically approaching the maximum turbulent Nusselt number (see Fig. 2) [25] (p. 47).

To model the dependence of the particle- and gas-convective Nusselt numbers on excess fluidization velocity, Molerus and Wirth used the maximum particle-convective (laminar) and gas-convective (turbulent) Nusselt numbers $\mathrm{Nu_{max}}$ as system properties [35] (pp. 78–79) and added damping functions $d(\pi_5)$ to account for the shape of the curves shown in Fig. 2 [36] (pp. 56, 62).

$$\mathrm{Nu} = \mathrm{Nu_{pc}} + \mathrm{Nu_{gc}} = \mathrm{Nu_{max,pc}} d_{\mathrm{pc}}(\pi_5) + \mathrm{Nu_{max,gc}} d_{\mathrm{gc}}(\pi_5) \tag{7}$$

The maximum gas-convective Nusselt number $\mathrm{Nu_{max,gc}} = \mathrm{Nu_{max,turb}}$ [25] (p. 45), [36] (p. 64) and its damping function $d_{\mathrm{gc}}(\pi_5)$ [36] (p. 56) are defined as

$$\mathrm{Nu_{max,gc}} = G_1 (\pi_3 \pi_4)^{1/3}$$

$$d_{\mathrm{gc}}(\pi_5) = (1 + G_2 \pi_6 / \pi_5)^{-1} \tag{8}$$

where the constants of gas convection $G_1 = 0.165$ and $G_2 = 0.05$ were determined from the evaluation of experiments [36] (p. 56). Gas convection plays only a minor role in this study.

Particle-convective heat transfer is characterized by the transport of particles to the heat transfer surface, the exchange of thermal energy between the particles and the surface through a thin layer of gas by thermal conduction, and the transport of particles away from the heat transfer surface [25] (p. 39). Consequently, the maximum particle-convective Nusselt number $\mathrm{Nu_{max,pc}}$ is composed of two resistances in series, a gas film resistance and a particle transport resistance [25] (p. 42). Molerus and Wirth also added a turbulence function $t(\pi_5)$ to account for increased particle transport resistance with increasing excess fluidization velocity in the mixed laminar/turbulent regime [36] (pp. 63–64).

$$\mathrm{Nu_{max,pc}} = P_1 \frac{\pi_7}{1 + \pi_2 t(\pi_5)} \tag{9}$$

The particle convection constant $P_1 = 0.125$ was again determined from the evaluation of experiments [36] (p. 64). The constant 1 in the denominator of Eq. 9 represents gas layer resistance, which is comprised of the laminar flow length scale l_{lam} and gas thermal conductivity k_g already included in the Nusselt number $\mathrm{Nu_{max,pc}} = \mathrm{Nu_{max,lam}} = h_{\mathrm{max,pc}} l_{\mathrm{lam}} / k_g$ [25] (p. 42).

The factor π_2 in Eq. 9 represents the (minimal or basic) particle transport resistance [35] (pp. 80–81). Under laminar flow conditions, a horizontal shear force occurs close to the heat transfer surface, dragging the particles away from it and causing their exchange [33] (pp. 12–15). An increased vertical particle velocity, caused by increased fluidization [35] (p. 81), also increases the shear force [33] (pp. 12–13) and thus particle exchange and wall-to-bed heat transfer [33] (p. 16). However, the particles' own inertia limits the velocity with which particles can be carried away from the heat transfer surface, resulting in the asymptotic approach of the maximum wall-to-bed HTC (Nusselt number $\mathrm{Nu_{max,lam}}$) with increasing excess fluidization velocity [35] (pp. 81–82), as shown in Fig. 2. The particle transport resistance π_2 hides this maximum particle velocity w_{max} in a particle Peclet number Pe [37] (pp. 146, 150) that relates the two resistances to heat transfer in the fluidized bed. As described earlier in this section, this occurs through (1) thermal energy transported to/from the heat transfer surface by a moving particle and (2) thermal conduction through a layer of gas per particle cross-section [35] (pp. 80–81).

$$\mathrm{Pe} = \frac{\rho_p c_p d_p^3 w_{\mathrm{max}}}{k_g d_p^2} = \frac{\text{heat capacity transport}}{\text{thermal conduction}} = \frac{\rho_p c_p d_p}{k_g} w_{\mathrm{max}} \tag{10}$$

Using dimensional analysis, the maximum particle velocity w_{max} can be derived from its influencing factors and is proportional to [35] (p. 81)

$$w_{max} \propto \frac{2\mu_g}{\rho_p d_p} \tag{11}$$

Replacing w_{max} in Eq. 10 with Eq. 11 yields the pi-factor $\pi_2 = k_g/\left(2c_p\mu_g\right)$, canceling out the particle density ρ_p and diameter d_p when the particle convective heat transfer is at its maximum in the purely laminar heat transfer regime [35] (p. 81).

The turbulence function $t(\pi_5)$ in Eq. 9 is used to "interpolate" between the purely particle-convective and the purely gas-convective regimes in the mixed particle convective/gas convective case [36] (pp. 55, 64):

$$t(\pi_5) = 1 + P_2\pi_7^2\pi_4^{1/2}\pi_5\pi_6 \tag{12}$$

where the constant $P_2 = 0.28$ [36] (p. 64). A greater excess fluidization velocity π_5 and a greater minimum fluidization velocity π_6 (caused by a greater Archimedes number Ar [29], p. 69) increase the value of the turbulence function $t(\pi_5)$ in Eq. 12 [36] (p. 64). Hence, the particle transport resistance π_2 in Eq. 9 increases with increasing Archimedes numbers Ar and excess fluidization velocities π_5, resulting in the shape of the curve for the mixed laminar/turbulent regime shown in Fig. 2.

The damping function $d_{pc}(\pi_5)$ describes the dependence of particle convection on the excess fluidization velocity [36] (p. 62):

$$d_{pc}(\pi_5) = \left(1 + P_3(\pi_6/\pi_5)^{1/3}\pi_5^{-1}\right)^{-1} \tag{13}$$

with $P_3 = 33.3$ [36] (p. 64). As mentioned in Section 2.1, π_5 includes the factor $\left(\rho_p c_p/(k_g g)\right)^{1/3}$, relating the particle transport and gas layer resistances [36] (p. 62). The inclusion of π_6 in Eq. 13 accounts for the additional influence of particle diameter on the fluidization velocity dependence of particle convection [36] (p. 62).

Combining Eqs. 5–12, Molerus and Wirth's entire correlation is structured as follows [36] (p. 64):

$$\pi_1 = P_1\frac{\pi_7}{1+\pi_2 t(\pi_5)}d_{pc}(\pi_5) + \mathrm{Nu}_{gc} \tag{14}$$

$$\pi_1 = P_1\frac{\pi_7}{1+\pi_2\left(1+P_2\pi_7^2\pi_4^{1/2}\pi_5\pi_6\right)}\left(1+P_3(\pi_6/\pi_5)^{1/3}\pi_5^{-1}\right)^{-1} + G_1(\pi_3\pi_4)^{1/3}(1+G_2\pi_6/\pi_5)^{-1}$$

with $P_1 = 0.125$, $P_2 = 0.28$, $P_3 = 33.3$, $G_1 = 0.165$, and $G_2 = 0.05$, as described below Eqs. 7, 8, and 11.

The correlation in Eq. 14 is valid for Archimedes numbers Ar between 10^2 and 10^5 [36] (pp. 64–65), i.e. in the mixed laminar/turbulent heat transfer regime, as described above. The correlation does not include the impact of radiative heat transfer, which is considered insignificant for particle sizes less than 500 µm at bed temperatures of up to 1050 K [36] (p. 55). The model was successfully tested using measurements of the wall-to-bed HTC at bed pressures between 0.1 MPa and 2 MPa, bed voidages at minimum fluidization conditions ε_{mf} between 0.3 and 0.53, and using different particle materials with a wide range of the specific heat capacity between 130 J/kgK and 1300 J/kgK [36] (p. 65).

2.3. Modifications to Molerus and Wirth's correlation

This section details how Molerus and Wirth's original correlation, described in Section 2.2, was modified to include the new dimensionless variables π_8 (impact of tube diameter), π_9 (impact of tube packing density), and π_{10} (impact of particle cross-flow).

2.3.1. Tube diameter

Molerus and Wirth demonstrated that reducing the diameter of a probe measuring the wall-to-bed HTC to a very small size results in an increase of the maximum achievable Nusselt number Nu_{max} by effectively increasing the frequency of particle exchange at the heat transfer surface [33] (pp. 15–17). This strongly suggests that a reduction in the tube diameter reduces the particle transport resistance π_2 in Eq. 9. Hence, the pi-factor $\pi_8 = d_t/l_{lam}$, representing the impact of the tube diameter d_t on the wall-to-bed HTC, was implemented as a size function $s(\pi_8)$ that decreases the particle transport resistance π_2 in Eq. 9.

$$\mathrm{Nu}_{max,pc} = P_1\frac{\pi_7}{1+\pi_2 t(\pi_5)s(\pi_8)} \tag{15}$$

Since the wall-to-bed HTC increases exponentially with decreasing probe size [33] (p. 17), the following form of the function $s(\pi_8)$ was chosen:

$$s(\pi_8) = 1 - \exp(-P_4\pi_8) \tag{16}$$

Different functional forms for $s(\pi_8)$ were also tested, which is reported in the data repository [23]. The size function $s(\pi_8)$ is limited between 0 when $\pi_8 = 0$ and 1 when $\pi_8 \to \infty$. When $\pi_8 = 0$, then $\pi_2 s(\pi_8 = 0) = 0$ suggests vanishing particle transport resistance when the tube diameter $d_t = 0$ is infinitesimally small. When $\pi_8 \to \infty$, then $\pi_2 s(\pi_8 \to \infty) = \pi_2$ implies sufficiently large heat transfer areas for Molerus and Wirth's original derivation of the particle transport resistance to still hold.

The extended model's estimated impact of the tube diameter on the maximum Nusselt number Nu_{max} was compared to the models listed in Table 4.

Note that the model from Molerus and Wirth in Table 4 does not refer to Molerus and Wirth's original correlation for the wall-to-bed HTC (the null hypothesis of this study); the model in Table 4 is instead based on a separate deliberation by Molerus and Wirth on the impact of "miniaturized" heat transfer measurement probes on the wall-to-bed HTC [33] (pp. 15–17). The null hypothesis does not account for the impact of the tube diameter on the wall-to-bed HTC.

2.3.2. Tube packing density

Several authors, such as Grewal and Saxena [21] (p. 371), Gel'perin et al. [40] (p. 142), and Natusch et al. [41] (p. 72), chose to add correction factors f_{tb} to the Nusselt number for single tubes Nu_{single} to account for the impact of densely packed tube banks on the wall-to-bed HTC.

$$\mathrm{Nu}_{tb} = \mathrm{Nu}_{single} f_{tb} \tag{17}$$

The tube bank correction factor f_{tb} therefore attenuates the (regular) Nusselt number for a single tube Nu_{single} to arrive at a Nusselt number for a tube bank Nu_{tb}. Using Molerus and Wirth's model, a different approach is proposed, as demonstrated in Fig. 3.

The enumerated points in Fig. 3 are obtained under the following conditions.

Table 4
Models for comparing the impact of the tube diameter d_t on the maximum Nusselt number Nu_{max} with the impact predicted by the extended model (Eqs. 14 and 15).

Model	Relation	d_t
Molerus & Wirth	$\mathrm{Nu}_{max} \propto 1 + 0.225\mathrm{e}-2\ \mathrm{m}/d_t$	–
Grewal & Saxena	$\mathrm{Nu}_{max} \propto d_t^{-0.21}$	28.6 mm
Merzsch et al.	$\mathrm{Nu}_{max} \propto d_t^{-0.3}$	33.7 mm

Max d_t refers to the maximum tube diameter investigated by the respective authors. Model sources: Molerus and Wirth [33] (p. 17), Grewal and Saxena [38] (pp. 108, 111, 113), Merzsch et al. [39] (p. 1043).

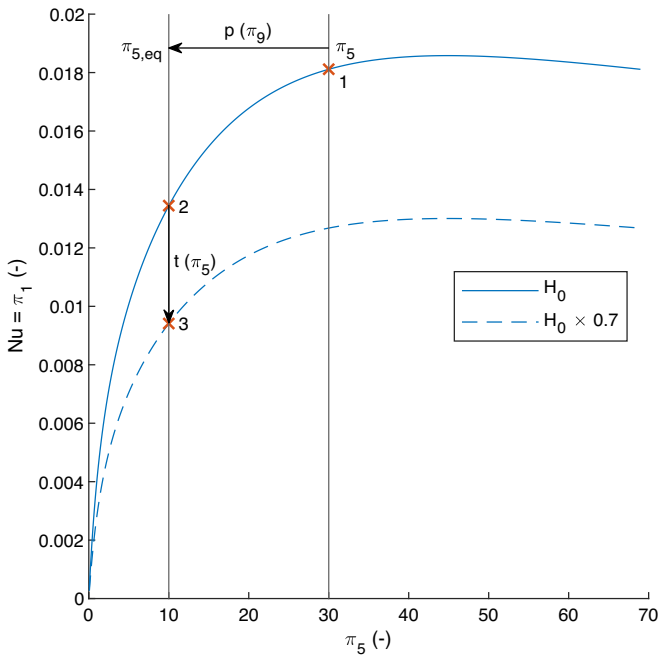

Fig. 3. Nusselt number Nu over dimensionless excess fluidization velocity π_5 according to Molerus and Wirth's original model H_0 and Molerus and Wirth's model reduced by a constant factor of 0.7, $H_0 \times 0.7$. Enumerated points are marked with a red x and explained in Section 2.3.2. Variables: $\pi_{5,eq}$ equivalent dimensionless excess fluidization velocity, $p(\pi_9)$ packing density function, $t(\pi_5)$ turbulence function. Conditions are identical to Fig. 2 at Archimedes number $Ar = 10^4$. Values are for demonstration purposes only and do not reflect the actual impact of a tube bank on the wall-to-bed HTC.

1. Without a tube bank, Molerus and Wirth's original model H_0 applies, resulting in a Nusselt number Nu at a given dimensionless excess fluidization velocity π_5. The dimensionless excess fluidization velocity π_5 is the driving force of vertical particle movement [33] (pp. 10–11), and its intensity and subsequent impact on the wall-to-bed HTC is taken into account in the particle-convective damping function $d_{pc}(\pi_5)$ in Molerus and Wirth's model (see Eq. 13).
2. With the inclusion of a densely packed tube bank, Chen [37] (p. 146) demonstrated that the intensity of the vertical circulation of particles in the fluidized bed is reduced without affecting the particle circulation pattern. A packing density function $p(\pi_9)$ therefore reduces the dimensionless excess fluidization velocity π_5 to produce an "equivalent" excess fluidization velocity $\pi_{5,eq}$ at which the vertical particle movement affected by the tube bank can by quantified by a modified particle-convective damping function $d_{pc}(\pi_{5,eq})$. This results in a reduction of the Nusselt number from point 1 to point 2 in Fig. 3.
3. At point 2, the turbulence function $t(\pi_5)$ at the (actual) dimensionless excess fluidization velocity π_5 still applies since it is the actual excess fluidization velocity that determines how turbulent the fluidized bed is. Since the value of the turbulence function $t(\pi_5)$ increases with increasing excess fluidization velocities π_5 (see Eq. 12), the value of $t(\pi_5)$ is disproportionally greater at the equivalent dimensionless excess fluidization velocity $\pi_{5,eq}$. This further reduces the achievable Nusselt number from point 2 to point 3 in Fig. 3.

This sequence of effects results in an overall reduction of the wall-to-bed HTC in the case of a tube bank in the fluidized bed, exemplified by $H_0 \times 0.7$ in Fig. 3, which is in effect identical to the use of a tube bank reduction factor f_{tb} to attenuate the Nusselt number for single tubes Nu_{single} in Eq. 17.

Based on the model described above, the tube packing density $\pi_9 = d_t/p_h$ was introduced as a packing density function $p(\pi_9)$ in the particle convective damping function $d_{pc}(\pi_5)$ in Eq. 13.

$$d_{pc}(\pi_5) = \left(1 + P_3(\pi_6/\pi_5)^{1/3}\pi_5^{-1}p(\pi_9)\right)^{-1} \tag{18}$$

The pi-factor $\pi_9 = d_t/p_h$ is naturally limited between the values 0 when $p_h \to \infty$ (single tube in a fluidized bed) and 1 when $p_h = d_t$ (the horizontal tube pitch p_h cannot be less than the tube diameter d_t, otherwise the tubes would intersect with each other). Therefore, the following form of the packing density function $p(\pi_9)$ was used:

$$p(\pi_9) = (1 - \pi_9)^{P_5} \tag{19}$$

The exponent P_5 (to be determined through the evaluation of heat transfer measurements) needs to be negative to ensure that an increased tube packing density π_9 reduces the dimensionless excess fluidization velocity π_5 in Eq. 18 to arrive at an equivalent dimensionless excess fluidization velocity $\pi_{5,eq}$, as described above.

The packing density function $p(\pi_9)$ in Eq. 18 only affects the particle-convective Nusselt number Nu_{pc} and has no impact on gas convection (see Eq. 7); this is justified since Molerus and Wirth [25] (pp. 46–47) did not identify an impact of tube packing density in the purely gas-convective heat transfer regime.

The extended model's estimated impact of the tube packing density π_9, as modeled in Eqs. 17 and 18, was compared to the alternative models listed in Table 5.

The vertical tube pitch p_v in the model from Gel'perin et al. in Table 5 is assumed to be equal to the horizontal tube pitch p_h in all model comparisons.

2.3.3. Particle cross-flow

Observations by the authors have indicated that particle cross-flow can have a significant influence on the wall-to-bed HTC. The inclusion of this effect into Molerus and Wirth's heat transfer model was derived from its description in Section 2.2.

2.3.3.1. General. The horizontal movement of particles adds to their regular vertical movement, thereby increasing the total velocity with which particles pass the heat transfer surface. Any increase in the wall-to-bed HTC due to particle cross-flow is therefore caused by increased particle convection.

The driving forces causing the horizontal and vertical movements of particles are different and independent from each other: a horizontal pressure gradient in the case of horizontal movement [42] (p. 86) and the excess fluidization velocity in the case of vertical movement [33] (pp. 10–11). This suggests that the modes of heat transfer are independent as well; hence, a new Nusselt number for particle cross-flow Nu_{cf} was added to Eq. 6.

$$Nu = Nu_{pc} + Nu_{gc} + Nu_{cf} \tag{20}$$

The general mechanism of particle convective heat transfer – that is, the transport of particles to and from the heat transfer surface and the exchange of thermal energy via thermal conduction through a layer of

Table 5
Models for comparing the impact of the tube packing density d_t/p_h on the maximum Nusselt number Nu_{max} with the impact predicted by the extended model (Eqs. 17 and 18).

Model	Relation
Grewal & Saxena	$Nu_{max} \propto 1 - 0.21(p_h/d_t)^{-1.75}$
Gel'perin et al.	$Nu_{max} \propto \left(1 - \frac{d_t}{p_h}\left(1 + \frac{d_t}{p_v + d_t}\right)\right)^{0.25}$
Natusch et al.	$Nu_{max} \propto (1 - d_t/p_h)^{0.25}$

Variables: d_t tube diameter, p_h horizontal tube pitch, p_v vertical tube pitch. Model sources: Grewal and Saxena [21] (p. 371), Gel'perin et al. [40] (p. 142), Natusch et al. [41] (p. 72).

gas between the particles and the surface, as described in Section 2.2 – does not change in the case of horizontal instead of vertical particle flow. Therefore, particle convection due to particle cross-flow also consists of two resistances in series: a gas film resistance and a particle transport resistance.

2.3.3.2. Particle transport resistance. Following the approach by Molerus and Wirth [35] (pp. 80–81), the particle transport resistance was derived from the particle Peclet number (see Eq. 10) using the mean horizontal particle velocity w_p.

$$\mathrm{Pe} = \frac{\rho_p c_p d_p}{k_g} w_p \tag{21}$$

In the case of regular vertical particle movement, the cause of particle exchange at the heat transfer surface is a horizontal particle velocity that is limited by the particles' inertia (see Section 2.2). In comparison, in the case of particle cross-flow the horizontal particle movement itself causes particle exchange, and particle cross-flow is practically unlimited. Eq. 21 therefore suggests that particle transport resistance should relate heat capacity transport, represented by $\rho_p c_p w_p$, to thermal conduction through the gas layer between surface and particle, represented by k_g, and should include the impact of the particle diameter d_p. These same requirements for characterizing the velocity dependence of particle convection are also fulfilled by the term $(\pi_6/\pi_5)^{1/3}\pi_5^{-1}$ in the particle convective damping function $d_{pc}(\pi_5)$ (Eq. 13), which describes the influence of the intensity of vertical particle movement as determined by the dimensionless excess fluidization velocity π_5 on the wall-to-bed HTC. Hence, by replacing π_5 with π_{10}, the term $(\pi_6/\pi_{10})^{1/3}\pi_{10}^{-1}$ describes the influence of the intensity of horizontal particle movement, determined by the dimensionless horizontal particle velocity π_{10}, on the wall-to-bed HTC. This term was therefore used as the particle transport resistance $r(\pi_{10})$ in the particle cross-flow Nusselt number.

$$\mathrm{Nu}_{cf} = C_1 \frac{\pi_7}{1 + r(\pi_{10})} = C_1 \frac{\pi_7}{1 + (\pi_6/\pi_{10})^{1/3}\pi_{10}^{-1}} \tag{22}$$

As in Eq. 9, the constant 1 in the denominator of Eq. 22 represents the gas layer resistance and the pi-factor π_7 accounts for the volumetric fraction of particles. The particle cross-flow constant C_1 needed to be determined through the evaluation of measurements.

2.3.3.3. Tube diameter. A reduction of the particle transport resistance by "miniaturization" of the heat transfer area, as discussed in Section 2.3.1, also applies in the case of particle cross-flow. As such, the size function $s(\pi_8)$ (Eq. 16) was added to Eq. 22 to decrease particle transport resistance with decreasing tube diameter.

$$\mathrm{Nu}_{cf} = C_1 \frac{\pi_7}{1 + r(\pi_{10})s(\pi_8)} \tag{23}$$

2.3.3.4. Turbulence. As discussed in Section 2.2 and shown in Fig. 2, the fluidized bed moves from a mixed laminar/turbulent flow regime to a purely turbulent regime with increasing excess fluidization velocity in the case of moderate Archimedes numbers Ar between 10^2 and 10^5.The turbulence function $t(\pi_5)$ in Eq. 12 is used to increase the particle transport resistance π_2 in Eq. 9 with increasing excess fluidization velocity to model this effect. Given that (regular) particle convection does not play a role in the purely turbulent flow regime, it was reasonable to assume that no particle movement of any kind (horizontal or vertical) contributes to heat transfer in this regime. Therefore, the turbulence function $t(\pi_5)$ was also added to Eq. 23 to affect the particle transport resistance of particle cross-flow.

$$\mathrm{Nu}_{cf} = C_1 \frac{\pi_7}{1 + r(\pi_{10})s(\pi_8)t(\pi_5)} \tag{24}$$

2.3.3.5. Relative contribution. How much an additional horizontal velocity component can contribute to the total particle velocity depends on the vertical particle velocity. Similar to the turbulence function $t(\pi_5)$ in Eq. 12, a damping function $d_{cf}(\pi_5)$ was therefore added to Eq. 24 to increase the particle transport resistance $r(\pi_{10})$ when the vertical particle velocity, determined by the dimensionless excess fluidization velocity π_5, is large.

$$\mathrm{Nu}_{cf} = C_1 \frac{\pi_7}{1 + r(\pi_{10})s(\pi_8)t(\pi_5)d_{cf}(\pi_5)} \tag{25}$$

The structure of the damping function $d_{cf}(\pi_5)$ was derived from its influencing factors:

- Vertical particle velocity, determined by π_5 [35] (p. 81)
- Horizontal particle velocity π_{10}
- The packing density function affecting vertical particle velocity (see Section 2.3.2), $p(\pi_9) = (1 - \pi_9)^C$ with exponent C

Furthermore, the damping function $d_{cf}(\pi_5)$ needed to approach 1 when $\pi_5 = 0$ (total particle velocity is completely horizontal) and approach infinity when $\pi_5 \to \infty$ (negligible impact of horizontal particle flow compared to vertical particle flow). Therefore, the following functional form of $d_{cf}(\pi_5)$ was chosen.

$$d_{cf}(\pi_5) = 1 + \pi_5^{C_2}\pi_{10}^{C_3}(1 - \pi_9)^{C_2 P_5 3/4} \tag{26}$$

The constants C_2 and C_3 needed to be determined through evaluation of experiments. The exponent of the packing density function $p(\pi_9) = (1 - \pi_9)$ was coupled with the exponent of the dimensionless excess fluidization velocity π_5, ensuring that the impact of the packing density function $p(\pi_9)$ on the dimensionless excess fluidization velocity π_5 is the same as in the purely particle-convective case (see Eqs. 17 and 18 for the relation between the exponents of $p(\pi_9)$ and π_5).

The functional form of $d_{cf}(\pi_5)$ in Eq. 26 is similar to that of the turbulence function $t(\pi_5)$ in Eq. 12. Other functional forms of $d_{cf}(\pi_5)$ were also tested, which is described in the data repository [23]. The functional form in Eq. 26 yielded the best results.

2.4. Secondary data

Measurements of the wall-to bed HTC were needed to evaluate the modifications of Molerus and Wirth's original correlation that model the impact of the tube diameter and tube packing density and to identify values for the missing constants and exponents (Sections 2.3.1 and 2.3.2, Eqs. 14–18). A wide variety of data was necessary to enable investigation of variations in all pi-factors affecting particle-convective heat transfer, which includes all pi-factors in Table 3 except π_3, which only affects gas convection (see Eqs. 7 and 13). Since the test rig used in this study did not allow for such variability, secondary data from previously published work was collected.

The following inclusion criteria were used in the search for usable measurements of the wall-to-bed HTC.

- The Archimedes number Ar must be below 10^5 for particle convection to play a significant role (as described in Section 2.2).
- All influencing factors of wall-to-bed heat transfer (Table 1) must be reported or can be derived from other reported parameters. In particular, the fluidization gas and particles must be substances with readily available heat capacity functions. Otherwise, the pi-factors in Table 1 cannot be calculated.
- The fluidized bed must include an immersed heat exchanger that consists of a staggered array of tubes (the focus of this study).
- Measurements of the wall-to-bed HTC must consider different tube diameters and/or tube packing densities to enable investigation of their variations.

- There must be no particle cross-flow, the impact of which on the wall-to-bed HTC was investigated using a separate test rig.

Table 6 summarizes the identified data sources.

Table 6 demonstrates that only the dataset from Grewal and Saxena [21] had a large number of observations, varied all pi-factors relevant to particle convection, and showed a wide range of Archimedes numbers Ar over two orders of magnitude. It was therefore used as the primary data source to evaluate the modifications of Molerus and Wirth's correlation and identify the missing constants and exponents for particle convective heat transfer. The results were then tested against the other datasets in Table 6.

Although the dataset from Kim [44] does not vary the tube diameter or tube packing density (π_8 and π_9) as shown in Table 6, it was still included in this study to test the results. The dataset from Eder et al. [43] included an additional 17 observations with a particle cross-flow, which were used to test the modifications adding the effect of particle cross-flow to Molerus and Wirth's correlation (Section 2.3.3).

All data collected for this study is available in the data repository [23]. The repository also includes a more detailed analysis of the collected data's ranges and variations in different factors.

2.5. Test rig

The impact of particle cross-flow on the wall-to-bed HTC was investigated using a test rig able to create a predefined particle cross-flow across an immersed heat exchanger consisting of a staggered array of horizontal tubes. Its technical design is described in Section 2.5.1, and the design of experiments is covered in Section 2.5.2.

2.6. Design

A sketch of the test rig and its measurement scheme is shown in Fig. 4.

The fluidized bed was about 2.25 m long and 0.5 m wide. The bed level above the fluidization gas distributor floor was about 0.5 m. Silicon dioxide (SiO_2) particles with a density ρ_p of 2650 kg/m^3 [48] (p. 344), porosity at minimum fluidization conditions ε_{mf} of 0.45, sphericity φ_S of 0.8, and mean diameter d_p of 175 μm were used.

A screw conveyor with a linear characteristic was utilized to add a specific mass flow of particles to one side of the fluidized bed. The particles traveled across the immersed heat exchanger to the other side, where they flowed over a weir to leave the fluidized bed again. The heat transfer measurement probe was located in the bed's center, and baffles above and below the probe delineated the flow area for the particles. A sintered plate distributed the fluidization gas across the fluidized bed, and orifice plates were used to measure the fluidization gas flow. A bed level control system [49] ensured that the heat exchanger was covered by only a minimum number of particles.

The test rig was originally used as a fluidized bed heat exchanger (FBHE) in a pilot plant of a thermal energy storage (TES) system. Hence, the tube arrays to the left and right of the heat transfer measurement probe were active heat exchangers using supercritical carbon dioxide (sCO_2) as heat transfer fluid (HTF). The heat exchangers were used to heat the fluidized bed to a specific temperature during the experiments. All tubes, including the heat transfer measurement probe, had helical fins welded to the outside (fins are not depicted in Fig. 4). Heat transfer measurements were adjusted for fin efficiency [50] (pp. 1273–1274) to make them comparable to heat transfer measurements using plain tubes.

The heat transfer measurement probe consisted of a tube with an inserted electric heating cartridge with a rated power of 4 kW_{el}. Ceramic insulators with a low thermal conductivity were used as the probe's bearings to ensure minimal heat transfer to the fluidized bed's walls. The probe's length (identical to the fluidized bed's width) was 500 mm, which limited the influence of wall effects on the measurements.

The bed temperature T_{bed} was measured at four locations equidistant to the tubes surrounding the heat transfer measurement probe (Fig. 4b). The probe's surface temperature T_{surf} was measured using a sensor directly attached to the probe's wall (Fig. 4c). By measuring the electric power P_{el} of the heating cartridge, the wall-to-bed HTC was calculated as [6] (p. 7)

$$h = \frac{P_{el}}{A\left(T_{surf} - T_{bed}\right)} \tag{27}$$

where A is the probe's outside heat transfer area accounting for fin efficiency, as mentioned above.

Detailed descriptions of the test rig, including design drawings; photographs; process flow diagrams of the surrounding pilot plant; data sheets of sensors, devices, and materials such as the particles; and a detailed description of the calculations are available in the data repository [23].

2.6.1. Experimental design

Similar to the selection of secondary data (Section 2.4, Table 6), operating point parameters of the test rig during heat transfer experiments with particle cross-flow were chosen to reflect a wide range of variations of different pi-factors. The chosen parameter variations and their impacts on pi-factors are summarized in Table 7.

Variations of the bed temperature T_{bed} primarily resulted in different thermo-physical properties of the particles and fluidization gas, which impacted $\pi_2 \ldots \pi_4$ and π_6 (dimensionless minimum fluidization velocity), as indicated in Table 7. Bed temperature variations had a secondary effect on π_5 (dimensionless excess fluidization velocity) and π_{10} (dimensionless mean horizontal particle velocity), which were varied directly by varying the relative excess fluidization velocity w_e/w_{mf} and the mean horizontal particle velocity w_p.

Since changing the particles and the configuration of the heat exchanger in the test rig was not feasible, the pi-factors π_7 (volume fraction of particles at minimum fluidization conditions) and π_9 (tube packing density) remained constant during all experiments. Bed temperature variations led to secondary variations of $\pi_8 = d_t/l_{lam}$ (relative contact time), although the tube diameter d_t was left unchanged. Variations of these pi-factors were already covered by the collected secondary data (Section 2.4, Table 6).

In addition to the parameter variations listed in Table 7, the control strategy of the electric heating cartridge was varied (see Section 2.5.1): half the experiments were conducted with a constant electric power P_{el} of about 1.1 kW_{el}, while in the other half the electric power was set in a closed-loop control system to achieve a temperature difference between the probe's surface and the fluidized bed $T_{surf} - T_{bed}$ of 100 K. This enabled the identification of a possible difference between the two driving forces of heat transfer in Eq. 27, namely the electric power P_{el} and the temperature difference $T_{surf} - T_{bed}$.

All parameters were varied approximately equally between all possible combinations of variations in Table 7 and different heating cartridge control strategies. A total of 75 measurements were conducted. All data is available in the data repository [23].

Table 6
Summary of secondary data sources. Ar denotes the range of Archimedes numbers.

Authors	Observations	Variations	Ar
Eder et al. [43]	6	π_1, π_5, π_8, π_9	1.8e2
Grewal & Saxena [21]	143	π_1, π_2, $\pi_4 \ldots \pi_9$	4.4e2…1.2e4
Kim et al. (2003) [44]	22	π_1, π_5	1.3e3
Kim & Kim (2013) [45]	33	π_1, $\pi_4 \ldots \pi_6$, π_8	1.3e3…9.3e3
Olsson & Almstedt [46]	8	π_1, $\pi_4 \ldots \pi_6$, π_8	3.3e4…6.5e4
Wiman & Almstedt [47]	24	π_1, $\pi_4 \ldots \pi_6$, π_8, π_9	8.3e3…6.6e4

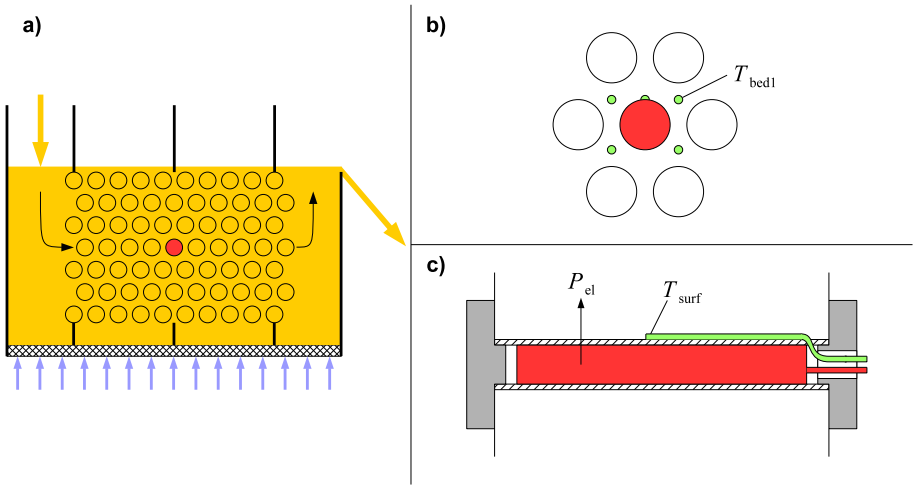

Fig. 4. Test rig schematics, a) cross-section of the fluidized bed, b) detailed arrangement of temperature sensors, c) cross-section through the heat transfer measurement probe. Orange areas represent the fluidized bed, checkered areas the sintered plate, red areas the electric heater, green areas temperature sensors, and gray areas ceramic insulators. Orange and black arrows in subfigure a) illustrate particle flows, blue arrows show flow of fluidization gas. Large circles represent heat exchanger tubes. Variables: T_{bed} bed temperature, T_{surf} surface temperature, P_{el} electric power. (For interpretation of the references to colour in this figure legend, the reader is referred to the web version of this article.)

Table 7
Test rig operating point parameters, their variations, and impacts on different pi-factors.

Parameter	Values	Primary Impact	Secondary Impact
T_{bed}	55°C 125°C 175°C	π_2 π_3 π_4 π_6	π_5 π_8 π_{10}
w_e/w_{mf}	1.6 2.1 2.8	π_5	–
w_p	1.4 mm/s 3.6 mm/s 7.1 mm/s 14.2 mm/s	π_{10}	–

Parameters: Bed temperature T_{bed}, excess fluidization velocity relative to minimum fluidization velocity w_e/w_{mf}, mean horizontal particle velocity w_p. See Table 3 for definitions of pi-factors.

2.7. Evaluation methods

Both the collected secondary data (Section 2.4) and the measurements from the test rig (Section 2.5) were used to evaluate the different modifications of Molerus and Wirth's heat transfer correlation (Section 2.3) and to identify values for the constants and exponents in Eqs. 14–15, 17–18, and 24–25.

The evaluation consisted of two steps in sequence.

1. Since both the modifications accounting for the impact of the tube diameter ($s(\pi_8)$ in Eq. 15) and the tube packing density ($p(\pi_9)$ in Eq. 18) affect the Nusselt number for (regular) particle convection Nu_{pc}, both modifications were evaluated simultaneously. The response variable $Nu_{pc} = Nu - Nu_{gc}$ was defined as the (collected) Nusselt number Nu reduced by the calculated gas convective Nusselt number Nu_{gc} according to Molerus and Wirth's original model (Eq. 8). The dataset from Grewal and Saxena [21] was used as the source for the Nusselt numbers Nu, as mentioned in Section 2.4.
2. The modifications accounting for the impact of particle cross-flow (Eqs. 24 and 25) only affect the cross-flow Nusselt number Nu_{cf}. The response variable $Nu_{cf} = Nu - Nu_{gc} - Nu_{pc}$ was defined as the (measured) Nusselt number Nu reduced by the calculated gas-convective Nusselt number Nu_{gc} (Eq. 8) and the particle-convective Nusselt number Nu_{pc} per the results from step 1. The data from the test rig experiments (Section 2.5) was used as the source for the Nusselt numbers Nu.

Combining Eqs. 4, 6, and 14 and inserting the turbulence function $t(\pi_5)$ (Eq. 12), the size function $s(\pi_8)$ (Eq. 16), and the modified particle convective damping function $d_{pc}(\pi_5)$ (Eqs. 17 and 18) yields the full equation of the response variable Nu_{pc} for step 1.

$$Nu_{pc} = P_1 \frac{\pi_7}{1 + \pi_2\left(1 + P_2\pi_7^2\pi_4^{1/2}\pi_5\pi_6\right)(1 - \exp(-P_4\pi_8))} \left(1 + P_3(\pi_6/\pi_5)^{1/3}\pi_5^{-1}(1-\pi_9)^{P_5}\right)^{-1} \quad (28)$$

The constants and exponents P_1, $P_3 \ldots P_5$ were affected by the modifications, meaning their values changed in the extended model compared to Molerus and Wirth's original model and therefore needed to be evaluated. The constant $P_2 = 0.28$ only applies to the turbulence function $t(\pi_5)$ (Eq. 12), which was unaffected by the modifications and therefore remains the same in the extended model.

Inserting the turbulence function $t(\pi_5)$ (Eq. 12), the size function $s(\pi_8)$ (Eq. 16), and the damping function for particle cross-flow $d_{cf}(\pi_5)$ (Eq. 26) into the equation for the particle cross-flow Nusselt number Nu_{cf} (Eq. 25) yields the full equation of the response variable Nu_{cf} for step 2.

$$\begin{aligned} Nu_{cf} &= C_1 \frac{\pi_7}{1 + (\pi_6/\pi_{10})^{1/3}\pi_{10}^{-1}t(\pi_5)s(\pi_8)d_{cf}(\pi_5)} \\ t(\pi_5) &= \left(1 + P_2\pi_7^2\pi_4^{1/2}\pi_5\pi_6\right) \\ s(\pi_8) &= (1 - \exp(-P_4\pi_8)) \\ d_{cf}(\pi_5) &= 1 + \pi_5^{C_2}\pi_{10}^{C_3}(1-\pi_9)^{C_2P_5 3/4} \end{aligned} \quad (29)$$

The constants and exponents $C_1 \ldots C_3$ needed to be evaluated; the particle-convective constants P_2, P_4 and P_5 were already determined in step 1.

The parameters P_1, $P_3 \ldots P_5$, $C_1 \ldots C_3$ were evaluated by fitting Eqs. 27 and 28 to their respective data using the Levenberg–Marquardt algorithm for non-linear regression [51] (pp. 624–627). The adjusted coefficient of determination R^2_{adj} was used to evaluate the goodness-of-fit, which measures how well the model is able to explain variance in the

data, adjusted for the number of regressors (values closer to 1 are better) [52] (pp. 125, 163). The regressors are the pi-factors in this study.

P-values were used to test individual parameters against the null hypothesis. The *p*-value of a parameter describes the probability that the mean of the residuals between the predictions made by the null hypothesis and the observed data is 0 [53] (p. 339). A low *p*-value for a parameter indicates that the modification of Molerus and Wirth's model associated with that parameter is able to model the intended effects. The chosen level of significance was below 1 %.

A detailed description of test statistics and their calculation is available in the data repository [23].

3. Results

This section presents the results of the non-linear regressions used to evaluate the modifications of Molerus and Wirth's heat transfer model and fit various parameters to the available data, as described in Section 2.6.

3.1. Tube diameter and tube packing density

Eq. 28 of the response variable $\mathrm{Nu_{pc}}$ with $P_2 = 0.28$ is repeated here to highlight the parameters P_1, $P_3 \ldots P_5$ whose values needed to be identified.

$$\mathrm{Nu_{pc}} = P_1 \frac{\pi_7}{1 + \pi_2 \left(1 + 0.28\pi_7^2 \pi_4^{1/2} \pi_5 \pi_6\right)(1 - \exp(-P_4 \pi_8))} \left(1 + P_3 (\pi_6/\pi_5)^{1/3} \pi_5^{-1} (1 - \pi_9)^{P_5}\right)^{-1} \quad (30)$$

Fig. 5 shows the results of the non-linear regression to fit the parameters P_1, $P_3 \ldots P_5$ to the data.

Fig. 5 demonstrates that Molerus and Wirth's original correlation H_0 (the null hypothesis) is not able to explain the data well: the adjusted coefficient of determination R^2_{adj} is below 0.5, and most measurements are overestimated. In comparison, the extended model H_1 fits the data well, with the adjusted coefficient of determination R^2_{adj} close to 1, the majority of estimates within ±20 % of the measurements, and residuals centered around 0. This rejects the null hypothesis in favor of the extended model.

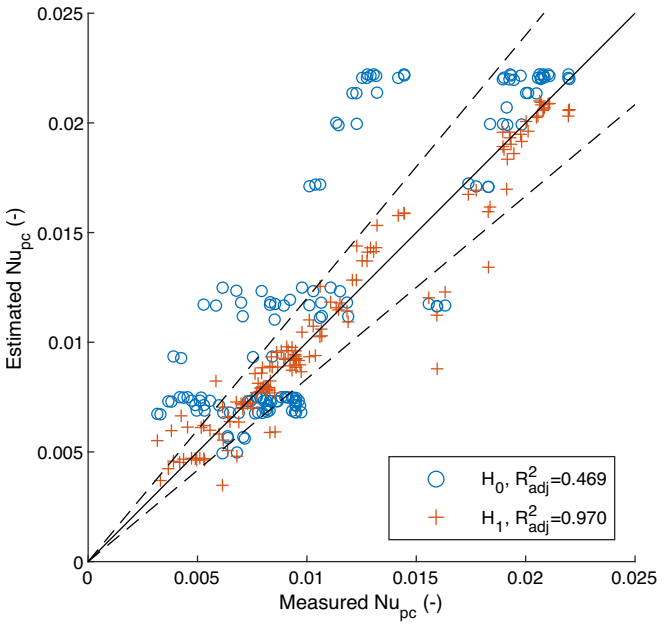

Fig. 5. Estimated vs. measured particle convective Nusselt number $\mathrm{Nu_{pc}}$ using the data from Grewal and Saxena [21]. Hypotheses: H_0 null hypothesis (Molerus and Wirth's original model) from Eq. 14, H_1 extended model from Eq. 30. R^2_{adj} refers to the adjusted coefficient of determination. The dashed lines indicate the ±20 % boundaries of estimates around the solid line representing perfect matches between measurements and model estimates.

Table 8
Fitted parameters P_1, $P_3 \ldots P_5$ of Eq. 30.

Parameter	H_0	Estimate	*P*-value
P_1	0.125	0.0691	4e-53
P_3	33.3	18.9085	2e-33
P_4	$\to\infty$	6.4582e-5	5e-39
P_5	0	−1.1523	8e-23

H_0 refers to the parameter values in Molerus and Wirth's original model in Eq. 14.

Table 8 shows the estimates of the fitted parameters in Eq. 30 and their *p*-values.

All parameters P_1, $P_3 \ldots P_5$ in Table 8 have very low *p*-values, suggesting a significant influence of their respective functional parts on the overall results and successful modeling of the intended effects. The estimates of both P_1 and P_3 are approximately 45 % smaller than their respective values in Molerus Wirth's original model H_0, which suggests a lower achievable maximum wall-to-bed HTC (P_1) and a lower impact of excess fluidization velocity on the wall-to-bed HTC (P_3).

3.2. Particle cross-flow

The response variable $\mathrm{Nu_{cf}}$ from Eq. 29 is repeated here with the previously determined parameters $P_2 = 0.28$, $P_4 = 6.46\mathrm{e}-5$, and $P_5 = 1.1523$ (Table 8).

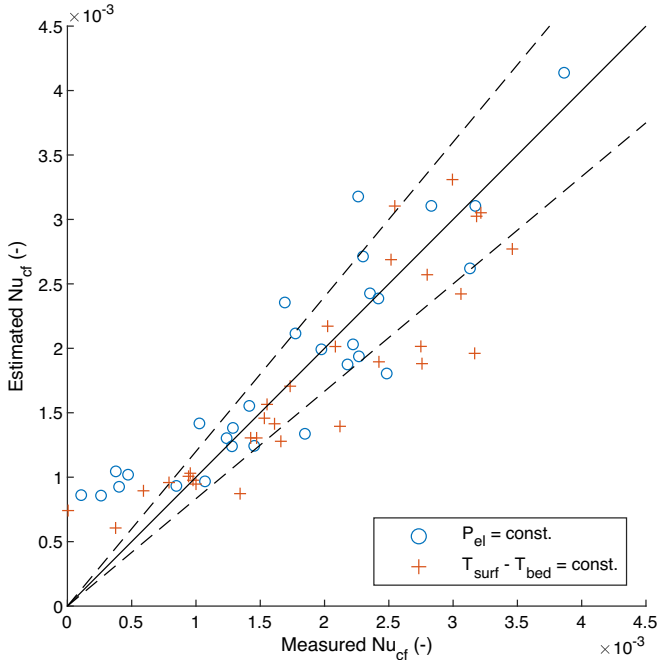

Fig. 6. Estimated vs. measured particle cross-flow Nusselt number $\mathrm{Nu_{cf}}$ using the data collected from the test rig (Section 2.5) and the model from Eq. 31. Control strategies: constant electric power P_{el} of the probe's heating cartridge, constant temperature difference between the tube's surface and the surrounding fluidized bed $T_{\mathrm{surf}} - T_{\mathrm{bed}}$. The dashed lines indicate the ±20 % boundaries of estimates around the solid line representing perfect matches between measurements and model estimates.

$$\begin{aligned} \mathrm{Nu}_{\mathrm{cf}} &= C_1 \frac{\pi_7}{1 + (\pi_6/\pi_{10})^{1/3} \pi_{10}^{-1} t(\pi_5) s(\pi_8) d_{\mathrm{cf}}(\pi_5)} \\ t(\pi_5) &= \left(1 + 0.28 \pi_7^2 \pi_4^{1/2} \pi_5 \pi_6\right) \\ s(\pi_8) &= (1 - \exp(-6.46\mathrm{e}-5\,\pi_8)) \\ d_{\mathrm{cf}}(\pi_5) &= 1 + \pi_5^{C_2} \pi_{10}^{C_3} (1-\pi_9)^{C_2 0.8642} \end{aligned} \tag{31}$$

Fig. 6 shows the results of fitting the parameters $C_1 \ldots C_3$ to the test rig measurements (Section 2.5) using non-linear regression, as described in Section 2.6. The results are distinguished between different control strategies for the driving force of heat transfer in Eq. 27, as mentioned in Section 2.5.2.

Since Molerus and Wirth's model does not account for the influence of particle cross-flow on the Nusselt number, the null hypothesis in Fig. 6 is identical to all estimated particle cross-flow Nusselt numbers $\mathrm{Nu}_{\mathrm{cf}} = 0$. For the results of both control strategies combined, the adjusted coefficient of determination R^2_{adj} is 0.83 and there are a few outliers beyond the ±20 % boundaries, indicating a good fit. Only very low cross-flow Nusselt numbers appear to be grossly overestimated.

There is a small bias in the measurements between the two control strategies in Fig. 6: The measured particle cross-flow Nusselt numbers $\mathrm{Nu}_{\mathrm{cf}}$ were on average about 10.5 % higher when using the $T_{\mathrm{surf}} - T_{\mathrm{bed}} =$ const. control strategy compared to the $P_{\mathrm{el}} =$ const. control strategy. In the case of the controlled temperature difference, the surface temperature T_{surf} was on average about 35 K higher and the electric power P_{el} was about 600 W larger compared to the other experiments. The bed temperature T_{bed} was unaffected by the surface temperature.

Table 9 shows the values of the estimated parameters $C_1 \ldots C_3$ in Eq. 31.

The results from Fig. 6 and the low p-values of the parameters $C_1 \ldots C_4$ in Table 9 demonstrate the ability of each functional part in Eq. 31 to model the observed effects and reject the null hypothesis.

4. Discussion

Molerus and Wirth's correlation for the wall-to-bed HTC does not include the impact of tube diameter, packing density of tubes in a heat exchanger, or particle cross-flow. The results of this study demonstrate that Molerus and Wirth's correlation can be extended by additional dimensionless numbers to account for these influencing factors.

4.1. Interpretation of results

This section interprets the results from Section 3, largely by comparing the estimates made by the extended model (using the coefficients and exponents from Tables 8 and 9) to the collected primary data, secondary data (Section 2.4), and alternative models listed in Tables 4 and 5.

4.1.1. Comparison between Molerus and Wirth and the extended model

Fig. 7 compares the estimates of Molerus and Wirth's original model with the estimates of the extended model using the collected test rig data, which includes both the influence of an immersed tube bank as well as the impact of particle cross-flow (see Section 2.5).

Note that, for better visibility of the data, estimates and measurements in Fig. 7 do not include the estimated gas convective Nusselt number $\mathrm{Nu}_{\mathrm{gc}}$, which is identical in both Molerus and Wirth's original model and in the extended model (see Eqs. 14 and 20). Fig. 7 demonstrates that Molerus and Wirth's model H_0 severely overestimates the measurements, primarily by not accounting for the mechanism of a densely packed tube bank reducing the vertical particle velocity and, thereby, the particle convective Nusselt number $\mathrm{Nu}_{\mathrm{pc}}$. In contrast, the estimates of the extended model H_1 are all within ±20 % of the measured values and show a far smaller variability than the estimates from Molerus and Wirth's model H_0. The extended model H_1 not only accounts for a reduction of the particle convective Nusselt number $\mathrm{Nu}_{\mathrm{pc}}$ by the immersed tube bank, but also for an increase of the total Nusselt number Nu by the particle cross-flow. The particle cross-flow adds, on average, about 50 % of the (regular) particle convective Nusselt number $\mathrm{Nu}_{\mathrm{pc}}$ to the total Nusselt number Nu, demonstrating the significant impact of particle cross-flow on wall-to-bed heat transfer in fluidized beds, which is not accounted for by Molerus and Wirth's original model H_0.

Table 9
Fitted parameters $C_1 \ldots C_3$ of Eq. 31.

Parameter	H_0	Estimate	P-value
C_1	0	0.0369	9e-11
C_2	0	2.2173	5e-21
C_3	0	0.6554	7e-14

4.1.2. Comparison to secondary data

As described in Section 2.4, the dataset from Grewal and Saxena [21] was used to find values for the coefficients and exponents of the extended model using non-linear regression analysis. Fig. 8 compares the extended model's estimates to the other datasets listed in Table 6.

The left side of Fig. 8 shows that the extended model is able to estimate the observations from Olsson and Almstedt [46] and Wiman and Almstedt [47] fairly well, while there is a clear bias in the estimates compared to the other datasets. The majority of measurements from both Olsson and Almstedt and Wiman and Almstedt had Archimedes numbers Ar that were greater than 1e4 (see Table 6), and those measurements are also estimated well by Molerus and Wirth's original model as shown on the right side of Fig. 8. However, on average, Molerus and Wirth's model also overestimates the measurements, and its estimates show a greater variance quantified as the root mean square error (RMSE), as shown in Table 10. The extended model is therefore still considered a better fit for the data than Molerus and Wirth's original model even though values of the wall-to-bed HTC may be overestimated in some cases, in particular at lower Archimedes numbers. The most likely source of the bias in the extended model is the gas-convective Nusselt number $\mathrm{Nu}_{\mathrm{gc}} = \mathrm{Nu}_{\mathrm{max,gc}} d_{\mathrm{gc}}(\pi_5)$ in Eq. 7, which acts as an additive factor (bias) to the total Nusselt number Nu. The maximum gas convective Nusselt number $\mathrm{Nu}_{\mathrm{max,gc}}$ is a function of π_3 and π_4 (see Eq. 8). None of the datasets in Table 6 varied the pi-factor π_3 and most of the variations of the pi-factor π_4 were only minor since the value of $\pi_4 = \rho_{\mathrm{g}}/(\rho_{\mathrm{p}} - \rho_{\mathrm{g}})$ is dominated by particle density ρ_{p}, and the particles were not varied in these datasets. The apparent bias in the estimates at lower Archimedes numbers Ar (as shown in Fig. 8) suggests additional dependence of the maximum gas-convective Nusselt number $\mathrm{Nu}_{\mathrm{max,gc}}$ on the Archimedes number Ar and/or on configuration parameters of the immersed heat exchanger, which contradicts previous observations made by Molerus and Wirth [25] (pp. 46–47).

4.1.3. Impact of tube diameter

Fig. 9 compares the predictions made by the extended model and the models listed in Table 4 regarding the impact of tube diameter on the maximum Nusselt number $\mathrm{Nu}_{\mathrm{max}}$.

The models from Grewal and Saxena and Merzsch et al. only predict an increase in the maximum Nusselt number $\mathrm{Nu}_{\mathrm{max}}$ at tube diameters below the maximum tube diameter $d_{\mathrm{t,max}}$ investigated by them (see Table 4). In comparison, the extended model predicts that the relative increase of the maximum Nusselt number in Fig. 9 asymptotically approaches 1 when the tube diameter approaches infinity. This is a reasonable result and is similar to Molerus and Wirth's model.

All models in Table 4 predict that the maximum Nusselt number $\mathrm{Nu}_{\mathrm{max}}$ approaches infinity when the tube diameter d_{t} becomes infinitesimally small. However, it is more realistic that gas layer resistance always plays a role in limiting the particle-convective Nusselt number regardless of the probe size; this factor is considered by the extended

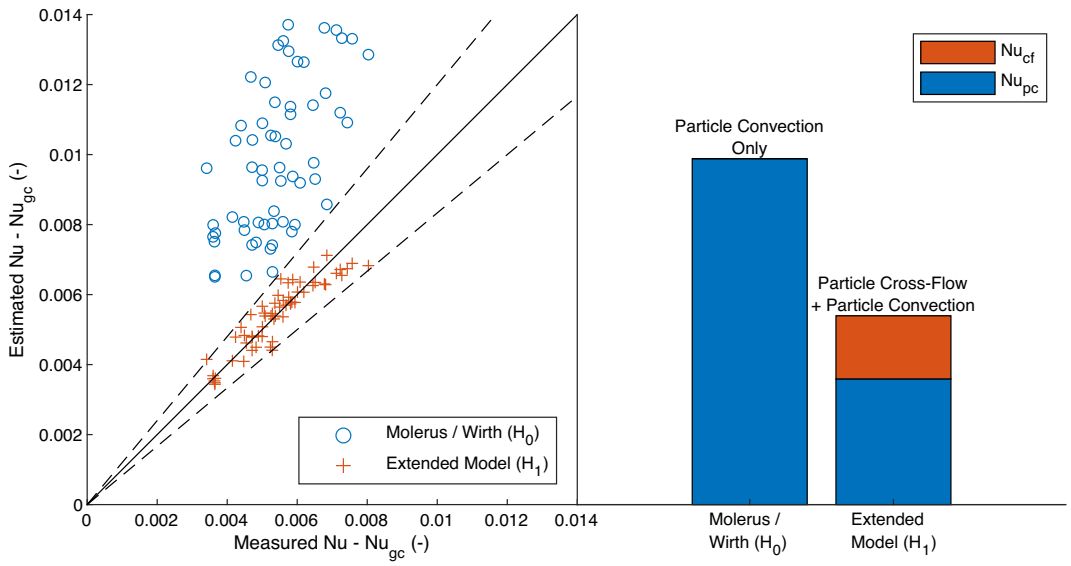

Fig. 7. Model estimates compared to the dataset collected from the test rig. Left side: estimated vs. measured Nusselt number Nu reduced by the estimated gas convective Nusselt number Nu_{gc}; Right side: compositions of the mean estimates of each model, consisting of the estimated particle convective Nusselt number Nu_{pc} and the estimated particle cross-flow Nusselt number Nu_{cf}. The left and right side of this graph share the same y-axis. The dashed lines on the left side indicate the ±20 % boundaries of estimates around the solid line representing perfect matches between measurements and model estimates. Hypotheses: H_0 Molerus and Wirth's original model (null hypothesis) from Eq. 14, H_1 extended model from Eqs. 20, 30, and 31.

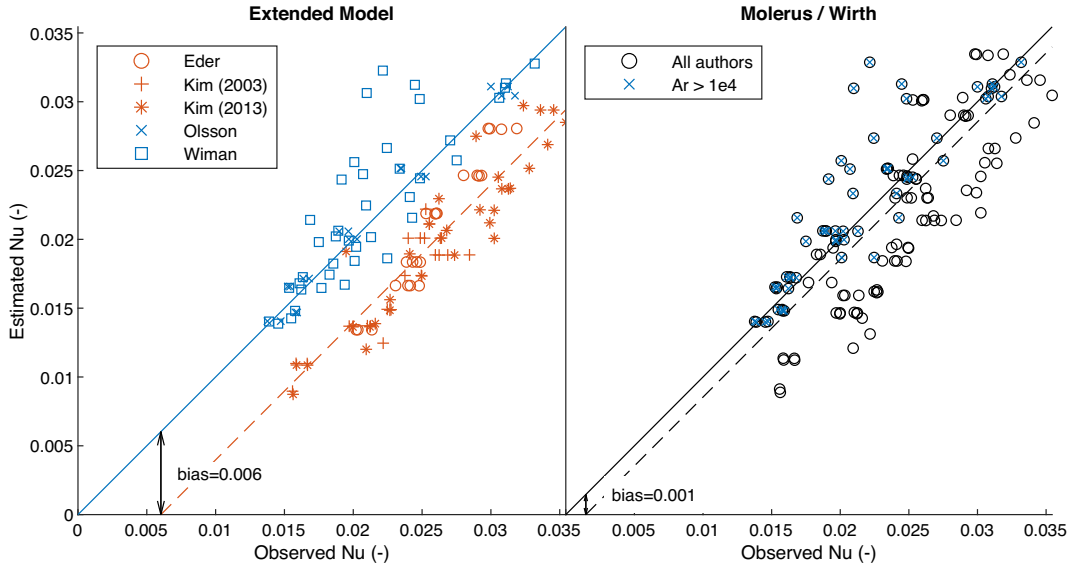

Fig. 8. Model estimates compared to different datasets (see Table 6). Left side: extended model; Right side: Molerus and Wirth's original model. Solid lines represent perfect matches between model estimates and observations, dashed lines are shifted by the indicated bias to produce a better fit between estimates and observations. Line colors match their fitted marker colors. Data points with a large Archimedes number Ar are marked separately on the right side.

Table 10
Goodness-of-fit parameters of different models in Fig. 8.

Model	Line Style	R^2_{adj}	RMSE
Extended, unbiased	–	0.6607	0.0028
Extended, biased	– –	0.8055	0.0020
Molerus & Wirth, unbiased	–	0.4037	0.0041
Molerus & Wirth, biased	– –	0.4801	0.0038

Line Style refers to either solid (–) or dashed (– –) lines in Fig. 8, R^2_{adj} is the adjusted coefficient of determination, and RMSE is the root mean square error.

model (see Eq. 15). The extended model's maximum Nusselt number Nu_{max} therefore approaches a finite value when the tube diameter becomes infinitesimally small.

Outside of very small tube diameters $d_t < 5$ mm, the extended model generally aligns well with the other models in Table 4, predicting a slightly larger relative increase of the maximum Nusselt number Nu_{max} at larger tube diameters than the other models. It also predicts a small impact of tube diameter beyond 40 mm, which is in line with Molerus and Wirth. Furthermore, the extended model predicts a greater relative increase in the maximum Nusselt number Nu_{max} at small tube diameters and greater Archimedes numbers Ar, although the absolute value of the maximum Nusselt number Nu_{max} still decreases with increasing Archimedes numbers (as shown in Fig. 2). None of the other models consider

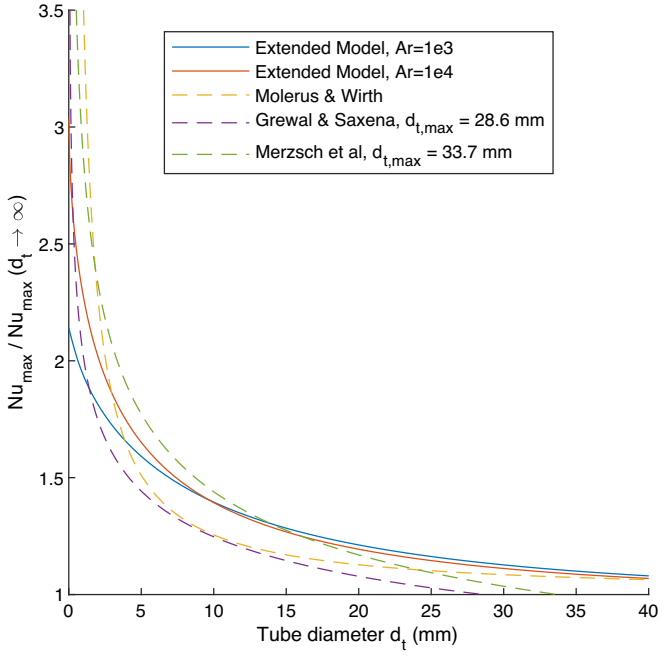

Fig. 9. Increase of the maximum Nusselt number Nu_{max} relative to the maximum Nusselt number at very large heat transfer areas $Nu_{max}(d_t \to \infty)$ with decreasing tube diameter d_t, according to different models (see Table 4). Some models cross the x-axis at the indicated tube diameter $d_{t,max}$. Parameters: Pressure p = 1e5 Pa, bed temperature T = 293.15 K, silica particles with bed voidage at minimum fluidization conditions ε_{mf} = 0.45, particle sphericity φ_S = 0.8, and the indicated Archimedes number Ar.

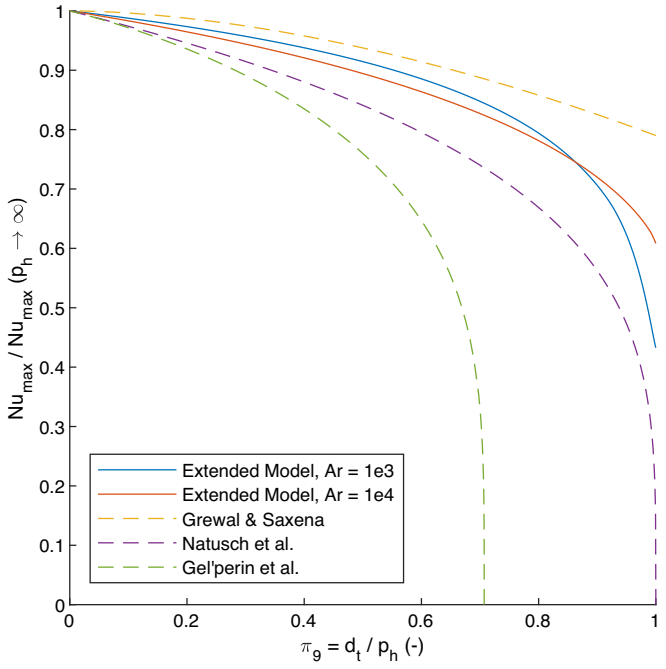

Fig. 10. Decrease of the maximum Nusselt number Nu_{max} with increasing tube packing density π_9 relative to the conditions of a single tube where the horizontal tube pitch p_h approaches infinity. See Table 5 for model definitions and references. Parameters: Pressure p = 1e5 Pa, bed temperature T = 293.15 K, silica particles with bed voidage at minimum fluidization conditions ε_{mf} = 0.45, particle sphericity φ_S = 0.8, tube diameter d_t = 25 mm, and the indicated Archimedes number Ar.

any factor other than the tube diameter itself to have an influence on the relative increase of the maximum Nusselt number.

4.1.4. Impact of tube packing density

Fig. 10 compares the impacts of tube packing density $\pi_9 = d_t/p_h$ on the maximum Nusselt number Nu_{max} in the extended model and the models listed in Table 5.

The models from Natusch et al. and Gel'perin et al. predict that the Nusselt number Nu approaches 0 when the tube packing density π_9 approaches 1. This is realistic since the tubes would block the entire cross-section of the bed if the tube packing density approached 1, stopping the fluidization. In contrast, while the extended model predicts that the particle-convective Nusselt number Nu_{pc} goes to 0 when the tube packing density π_9 approaches 1, the gas-convective Nusselt number Nu_{gc} is unaffected by the tube packing density π_9, resulting in a residual heat transfer in the form of gas convection when the tube packing density π_9 approaches 1. However, none of the secondary data collected in this study (Section 2.4) had a tube packing density π_9 greater than 0.6, and the extended model aligns well with the models from Grewal and Saxena and Natusch et al. at tube packing densities π_9 below 0.6.

The extended model also predicts that the impact of the tube packing density π_9 on the maximum Nusselt number Nu_{max} slightly depends on the Archimedes number Ar, which none of the other models do.

4.1.5. Contribution of particle cross-flow

The measured particle cross-flow Nusselt numbers Nu_{cf} shown in Fig. 6 comprised up to about 25 % of the total Nusselt number, making particle cross-flow a significant factor in wall-to-bed heat transfer. In contrast, Eder et al. [43] (p. 7426) did not find a significant influence of particle cross-flow on the wall-to-bed HTC. However, the extended model's total particle transport resistance r_{total} can reconcile both results (see also Eq. 25):

$$r_{total} = r(\pi_{10})s(\pi_8)t(\pi_5)d_{cf}(\pi_5) \tag{32}$$

Calculating the mean values for both the measurements from Eder et al. and from the test rig (Table 11) for each factor in Eq. 32 reveals that the (raw) particle transport resistance $r(\pi_{10})$ is about an order of magnitude greater in the measurements from Eder et al. than in the test rig measurements.

The lower (raw) particle transport resistance $r(\pi_{10})$ in the case of the test rig measurements is primarily owed to the greater mean horizontal particle velocities π_{10} compared to the measurements from Eder et al., which is also shown in Table 11. The mean values of the size function $s(\pi_8)$ and the turbulence function $t(\pi_5)$ are similar in both sources, with the test rig measurements having slightly smaller values. Eder et al. generally used greater excess fluidization velocities π_5 than the test rig measurements, resulting in greater values of the cross-flow damping function $d_{cf}(\pi_5)$. The combination of all factors resulted in a far greater total particle transport resistance r_{total} in the case of the measurements from Eder et al. compared to the test rig measurements, which is demonstrated in Fig. 11.

Fig. 11 shows that the total particle transport resistance r_{total} is generally about an order of magnitude greater in the measurements from Eder et al. than in the test rig measurements at equal excess fluidization velocities π_5. About half the measurements from Eder et al. were also conducted at greater excess fluidization velocities π_5 than the

Table 11
Mean values of π_{10} and the individual factors comprising the total particle transport resistance r_{total} in Eq. 32 across all measurements from the test rig and from Eder et al. [43].

Source	π_{10}	$r(\pi_{10})$	$s(\pi_8)$	$t(\pi_5)$	$d_{cf}(\pi_5)$
Test rig	1.71	1.29	0.48	1.08	25.9
Eder et al. [43]	0.31	10.9	0.58	1.11	92.7

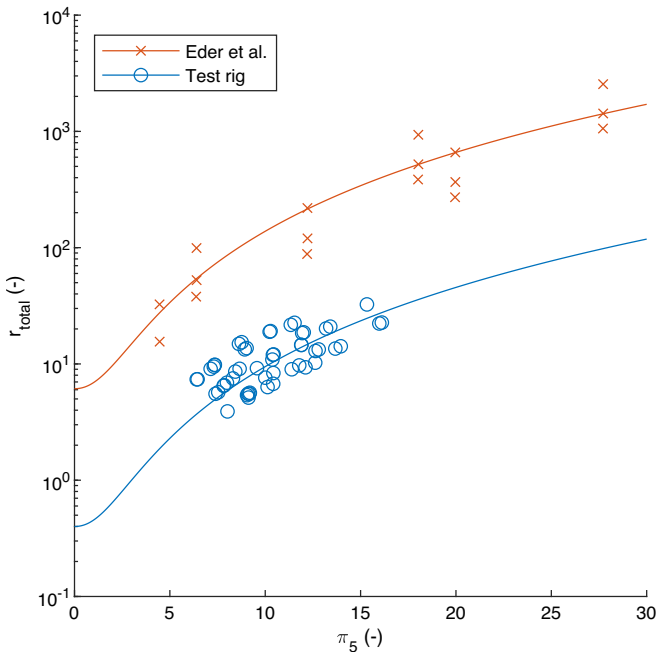

Fig. 11. Total particle transport resistance r_{total} (logarithmic scale) over dimensionless excess fluidization velocity π_5 for the measurements from Eder et al. [43] and from the test rig. The solid lines represent values of r_{total} calculated with the mean values of all relevant pi-factors for the respective source.

test rig measurements, resulting in a greater total particle transport resistance r_{total} due to greater values of the particle cross-flow damping function $d_{cf}(\pi_5)$ (see Eq. 32). As described in Section 2.3.3, the particle cross-flow damping function $d_{cf}(\pi_5)$ accounts for the relative impact of the horizontal movement of particles compared to their regular vertical movement. Fig. 11 indicates that the vertical particle velocity overshadows any additional particle movement in the horizontal direction in the case of the measurements from Eder et al. for a wide range of excess fluidization velocities, thereby rendering the particle cross-flow's contribution to the wall-to-bed HTC insignificant. Since the horizontal particle velocities are lower in the case of Eder et al. (see Table 11), the total particle transport resistances r_{total} in the measurements from Eder et al. are only comparable to the values obtained from the test rig measurements in the lowest range of excess fluidization velocities π_5. Hence, Eder et al. could have only attained significant contributions of the particle cross-flow on the wall-to-bed HTC at very low dimensionless excess fluidization velocities π_5, greater particle cross-flows (reduced $r(\pi_{10})$), and/or higher tube packing densities (reduced $d_{cf}(\pi_5)$) to limit the influence of vertical particle movement on the wall-to-bed HTC. The extended model accounts for these effects and can correctly predict the results from Eder et al.

4.1.6. Impact of control strategy

The results of the test rig measurements in Section 3.2 indicate that a higher surface temperature T_{surf} improves the wall-to-bed HTC independently from the bed temperature T_{bed}. It is plausible that the gas film resistance (factor 1 in Eqs. 8 and 21) is directly affected by the probe's surface temperature T_{surf}. As described in Section 2.2, the gas film resistance is proportional to the inverse of the fluidization gas's thermal conductivity $\propto k_g^{-1}$. The gas film temperature increases with the surface temperature, which results in a larger thermal conductivity of the gas film [54] (pp. 173–174), thereby reducing the gas film resistance. Neither the extended model nor Molerus and Wirth's original model account for a separate influence of the gas film's thermal conductivity independently from the bulk of the fluidized bed.

4.2. Implications

The extended model developed in this study provides a clearer understanding of how tube diameter, tube packing density, and particle cross-flow impact the wall-to-bed HTC in a fluidized bed, how these factors are influenced by other operating parameters (especially excess fluidization velocity), and how they influence each other.

A reduction in the tube diameter reduces the effective particle transport resistance, which improves wall-to-bed heat transfer. In contrast, a greater packing density of heat exchanger tubes slows the vertical transport velocity of particles, reducing wall-to-bed heat transfer. Particle cross-flow only has a significant impact on the wall-to-bed HTC at high horizontal particle velocities, low excess fluidization velocities, and/or high tube packing densities. The extended model also considers the impact of other operating parameters, such as the Archimedes number, on each of these factors.

The extended model can therefore be used as a single, comprehensive model in the design, optimization, and analysis of FBHEs of the type investigated in this study. It also enables a more precise design of experiments in future research to investigate individual influencing factors of the wall-to-bed HTC.

The observed impact of the surface temperature T_{surf} on the wall-to-bed HTC implies that different wall-to-bed HTCs occur when heating (high surface temperature) or cooling (low surface temperature) the fluidized bed at the same bed temperature T_{bed}.

4.3. Limitations

Although the interpretation of results in Section 4.1 demonstrated that the extended model developed in this study largely aligns with previously published models and datasets, some limitations to its reliability and generalizability still apply.

The development of the extended model was generally hampered by a lack of consistent data from a single source covering all the different influencing factors of wall-to-bed heat transfer in a fluidized bed. Different authors have used different methods for measuring the wall-to-bed HTC, which may have contributed to the bias seen in the extended model's estimates for some of the authors (see Section 4.1.2 and Fig. 8). Limitations of the test rig prohibited the use of more than one type of particle or tube bank configuration.

All the data used in this study was collected in the mixed particle/gas convective heat transfer regime. This made separate investigations of different effects more difficult, particularly regarding particle convection (with and without particle cross-flow) without the interference of gas convection. As described in Section 4.1.2, this interference is the most likely source of the bias in the extended model's estimates for fluidized beds with lower Archimedes numbers (Fig. 8).

Only the test rig measurements produced results revealing a significant contribution of particle cross-flow on the wall-to-bed HTC. Limitations in the test rig's design restricted the investigations to a single tube bank configuration and a single set of particles. Furthermore, all tubes in the test rig's tube bank had helical fins attached to their outside, making corrections necessary to be able to compare the results to those from other authors, as described in Section 2.5.1. Inaccuracies in these corrections may have introduced an unidentified bias in the test rig measurements.

As described in Section 4.1.4, the model incorrectly predicts residual heat transfer in the form of gas convection at very high tube packing densities since no impact of the tube packing density on the gas-convective Nusselt number was considered in this study.

Since the extended model is based on Molerus and Wirth's model for the mixed laminar/turbulent regime, the same range of operating conditions applies, as mentioned in Section 2.2:

- Archimedes number Ar between 10^2 and 10^5
- Mean particle diameter below 500 μm

- Bed temperature up to 1050 K

The extended model's parameters P_1 and P_3 (see Table 8) should also only be used in cases where the tube packing density π_9 is greater than 0.2, since the impact of tube packing density on wall-to-bed heat transfer is very small below this value (see Fig. 10). The original parameters from Molerus and Wirth's model (see Table 8) should be used in cases where $\pi_9 < 0.2$. The extended model is only valid for bubbling fluidized beds.

4.4. Future research

Based on the limitations discussed in Section 4.3, future research should primarily focus on producing consistent data of wall-to-bed HTCs varying a wide array of influencing factors, in particular tube diameter and tube packing density. Separate measurements for the purely particle convective, purely gas convective, and mixed particle/gas convective heat transfer regimes should be conducted by using particles of different sizes (as described in Section 2.2), thereby facilitating separate investigations of different effects in each regime. Furthermore, the impact of fins on the wall-to-bed HTC and their reciprocal influence on other influencing factors should be investigated separately as well.

Future model adaptations should include the impact of very high tube packing densities on the gas convective Nusselt number and the impact of the surface temperature on the wall-to-bed HTC.

5. Conclusion

While the correlation developed by Molerus and Wirth has been successfully used in estimating the wall-to-bed heat transfer coefficient in fluidized beds over a wide range of operating conditions, it does not account for the influence of an immersed tube bank or a cross-flow of particles. By introducing additional dimensionless factors, this study demonstrated that Molerus and Wirth's correlation can be extended to cover these influencing factors, resulting in a comprehensive model that is able to explain the individual impact of each factor on the wall-to-bed HTC. The extended model enables an improved understanding of the phenomena governing wall-to-bed heat transfer in a fluidized bed as well as better targeted research to further explore individual influencing factors. Furthermore, measurements and the extended model indicate that particle cross-flow only plays a significant role under specific conditions. Additional research is needed to produce more consistent data on wall-to-bed heat transfer coefficients in fluidized beds and enable further model adaptations.

Funding

The information, data, or work presented in this paper was funded in part by the Advanced Research Projects Agency-Energy (ARPA-E), U.S. Department of Energy, under Award Number DE-AR0000996. The views and opinions of authors expressed herein do not necessarily state or reflect those of the United States Government or any agency thereof.

The APC was funded by TU Wien Bibliothek.

CRediT authorship contribution statement

Stefan Thanheiser: Conceptualization, Methodology, Software, Validation, Formal analysis, Investigation, Data curation, Writing – original draft, Visualization.

Declaration of competing interest

The authors declare that they have no known competing financial interests or personal relationships that could have appeared to influence the work reported in this paper.

Acknowledgments

Luke Magyar and Brett Bowan (Echogen Power Systems) supported data collection; Timothy J. Held and Jason Miller (Echogen Power Systems) supported with technical and scientific advice; Gerhard Hofer and Tobias Pröll (BOKU University) supplied measured data; Viktoria Illyés (TU Wien) gave feedback on the manuscript; Markus Haider (TU Wien) supervised the project. The authors acknowledge TU Wien Bibliothek for financial support through its Open Access Funding Program.

Data availability

The data presented in this study is openly available in Zenodo at: https://doi.org/10.5281/zenodo.16748329
Software for data analysis is openly available in Zenodo at: https://doi.org/10.5281/zenodo.16748359

References

[1] D.E. Jia, Heat and mass transfer, in: J. Grace, X. Bi, N. Ellis (Eds.), Essent. Fluid. Technol, John Wiley & Sons, 2020, pp. 291–331, https://doi.org/10.1002/9783527699483.ch14.
[2] W.R.W. Daud, Fluidized bed dryers — recent advances, Adv. Powder Technol. 19 (2008) 403–418, https://doi.org/10.1016/S0921-8831(08)60909-7.
[3] G. Jiménez-García, R. Aguilar-López, R. Maya-Yescas, The fluidized-bed catalytic cracking unit building its future environment, Fuel 90 (2011) 3531–3541, https://doi.org/10.1016/j.fuel.2011.03.045.
[4] C. Wu, H. Yang, X. He, C. Hu, L. Yang, H. Li, Principle, development, application design and prospect of fluidized bed heat exchange technology: comprehensive review, Renew. Sust. Energ. Rev. 157 (2022) 112023, https://doi.org/10.1016/j.rser.2021.112023.
[5] E. Sette, D. Pallarès, F. Johnsson, Influence of bulk solids cross-flow on lateral mixing of fuel in dual fluidized beds, Fuel Process. Technol. 140 (2015) 245–251, https://doi.org/10.1016/j.fuproc.2015.09.017.
[6] S. Thanheiser, M. Haider, P. Schwarzmayr, Experimental investigation of the heat transfer between finned tubes and a bubbling fluidized bed with horizontal sand mass flow, Energies 15 (2022) 1316, https://doi.org/10.3390/en15041316.
[7] H.S. Mickley, D.F. Fairbanks, Mechanism of heat transfer to fluidized beds, AICHE J. 1 (1955) 374–384, https://doi.org/10.1002/aic.690010317.
[8] J.S.M. Botterill, K.A. Redish, D.K. Ross, J.R. Williams, The mechanism of heat transfer to fluidised beds, in: Proc. Symp. Interact. Fluids Part, Institution of Chemical Engineers, London, 1962, pp. 183–189.
[9] J.D. Gabor, Wall-to-bed heat transfer in fluidized and packed beds, Fluid. Fundam. Appl. 66 (1970) 76–86.
[10] P. Basu, Heat transfer, in: Combust. Gasif. Fluid. Beds, CRC Press, Boca Raton, 2006, pp. 173–210.
[11] O. Molerus, K.-E. Wirth, Historical remarks, in: Heat Transf. Fluid. Beds, Springer, Dordrecht, 1997, pp. 90–95, https://doi.org/10.1007/978-94-011-5842-8_12.
[12] H. Martin, M5 Heat Transfer in Fluidized Beds, in: VDI Heat Atlas, 2nd ed., Springer, Berlin, Heidelberg, 2010, pp. 1301–1310, https://doi.org/10.1007/978-3-540-77877-6_98.
[13] B.R. Andeen, L.R. Glicksman, Heat transfer to horizontal tubes in shallow fluidized beds, ASME Pap. 76 (1976) 1–8.
[14] V.A. Borodulya, V.G. Ganzha, A.I. Podberezsky, in: J.R. Grace, J.M. Matsen (Eds.), Heat Transfer in a Fluidized Bed at High Pressure, Fluidization, Springer, Boston, MA, 1980, pp. 201–207, https://doi.org/10.1007/978-1-4684-1045-7_17.
[15] Z. Bao, L. Duan, K. Wu, C. Zhao, An investigation on the heat transfer model for immersed horizontal tube bundles in a pressurized fluidized bed, Appl. Therm. Eng. 170 (2020) 115035, https://doi.org/10.1016/j.applthermaleng.2020.115035.
[16] N.S. Grewal, A generalized correlation for heat transfer between a gas—solid fluidized bed of small particles and an immersed staggered array of horizontal tubes, Powder Technol. 30 (1981) 145–154, https://doi.org/10.1016/0032-5910(81)80007-1.
[17] N.S. Grewal, S.C. Saxena, Heat transfer between a horizontal tube and a gas-solid fluidized bed, Int. J. Heat Mass Transf. 23 (1980) 1505–1519, https://doi.org/10.1016/0017-9310(80)90154-4.
[18] O. Molerus, K.-E. Wirth, Heat Transfer in Fluidized Beds, Springer, Dordrecht, 1997, https://doi.org/10.1007/978-94-011-5842-8.
[19] R. Chhabra, M.G. Basavaraj, Fluidisation, in: Part. Syst. Part. Technol, 6th ed., Butterworth-Heinemann, 2019, pp. 449–554, https://doi.org/10.1016/B978-0-08-101098-3.00010-X.
[20] G. Hofer, G. Schöny, J. Fuchs, T. Pröll, Investigating wall-to-bed heat transfer in view of a continuous temperature swing adsorption process, Fuel Process. Technol. 169 (2018) 157–169, https://doi.org/10.1016/j.fuproc.2017.09.024.
[21] N.S. Grewal, S.C. Saxena, Experimental studies of heat transfer between a bundle of horizontal tubes and a gas-solid fluidized bed of small particles, Ind. Eng. Chem. Process. Des. Dev. 22 (1983) 367–376, https://doi.org/10.1021/i200022a005.

[22] O. Molerus, K.-E. Wirth, Significant features of equation (7.17), in: Heat Transf. Fluid. Beds, Springer, Dordrecht, 1997, pp. 69–74, https://doi.org/10.1007/978-94-011-5842-8_8.
[23] S. Thanheiser, Extended Heat Transfer Model Dataset, 2025. https://doi.org/10.5281/zenodo.16748329.
[24] S. Thanheiser, Extended Heat Transfer Model Software, 2025, https://doi.org/10.5281/zenodo.16748359.
[25] O. Molerus, K.-E. Wirth, Heat transfer mechanisms in bubbling fluidized beds, in: Heat Transf. Fluid. Beds, Springer, Dordrecht, 1997, pp. 35–47, https://doi.org/10.1007/978-94-011-5842-8_4.
[26] S. Lechner, M. Merzsch, H.J. Krautz, Heat-transfer from horizontal tube bundles into fluidized beds with Geldart a lignite particles, Powder Technol. 253 (2014) 14–21, https://doi.org/10.1016/j.powtec.2013.10.041.
[27] S.C. Saxena, in: J.P. Hartnett, T.F. Irvine (Eds.), Heat Transfer between Immersed Surfaces and Gas-Fluidized Beds, Elsevier, 1989, pp. 97–190, https://doi.org/10.1016/S0065-2717(08)70212-0.
[28] V. Gnielinski, G7 Heat Transfer in Cross-Flow around Single Rows of Tubes and through Tube Bundles, in: VDI Heat Atlas, 2nd ed., Springer, Berlin, Heidelberg, 2010, pp. 725–730, https://doi.org/10.1007/978-3-540-77877-6_40.
[29] D. Kunii, O. Levenspiel, Fluidization and mapping of regimes, in: Fluid. Eng, 2nd ed., Butterworth-Heinemann, Boston, 1991, pp. 61–94, https://doi.org/10.1016/B978-0-08-050664-7.50009-3.
[30] J.R. Grace, Introduction, history, and applications, in: J. Grace, X. Bi, N. Ellis (Eds.), Essent. Fluid. Technol, John Wiley & Sons, 2020, pp. 1–9, https://doi.org/10.1002/9783527699483.ch1.
[31] D. Kunii, O. Levenspiel, Bubbling fluidized beds, in: Fluid. Eng, 2nd ed., Butterworth-Heinemann, Boston, 1991, pp. 137–164, https://doi.org/10.1016/B978-0-08-050664-7.50012-3.
[32] J.R. Grace, Hydrodynamics of bubbling fluidization, in: J. Grace, X. Bi, N. Ellis (Eds.), Essent. Fluid. Technol, John Wiley & Sons, 2020, pp. 131–152, https://doi.org/10.1002/9783527699483.ch7.
[33] O. Molerus, K.-E. Wirth, Particle migration at solid surfaces and heat transfer in bubbling fluidized beds, in: Heat Transf. Fluid. Beds, Springer, Dordrecht, 1997, pp. 5–17, https://doi.org/10.1007/978-94-011-5842-8_2.
[34] T. Szirtes, Systematic determination of complete set of products of variables, in: T. Szirtes, P. Rózsa (Eds.), Appl. Dimens. Anal. Model, 2nd ed., Butterworth-Heinemann, Burlington, 2007, pp. 163–179, https://doi.org/10.1016/B978-012370620-1.50014-9.
[35] O. Molerus, K.-E. Wirth, Physical background to convective heat transfer, in: Heat Transf. Fluid. Beds, Springer, Dordrecht, 1997, pp. 78–83, https://doi.org/10.1007/978-94-011-5842-8_10.
[36] O. Molerus, K.-E. Wirth, Prediction of heat transfer in bubbling fluidized beds at Ar $\leq$ 10^8, in: Heat Transf. Fluid. Beds, Springer, Dordrecht, 1997, pp. 55–68, https://doi.org/10.1007/978-94-011-5842-8_7.
[37] M.M. Chen, Solids motion and heat transfer in gas fluidized beds, in: F. Kreith, R. F. Boehm (Eds.), Direct-Contact Heat Transf, Springer, Berlin, Heidelberg, 1985, pp. 127–166, https://doi.org/10.1007/978-3-662-30182-1_8.
[38] N.S. Grewal, S.C. Saxena, Maximum heat transfer coefficient between a horizontal tube and a gas-solid fluidized bed, Ind. Eng. Chem. Process. Des. Dev. 20 (1981) 108–116, https://doi.org/10.1021/i200012a017.
[39] M. Merzsch, S. Lechner, H.J. Krautz, Heat-transfer from single horizontal tubes in fluidized beds: influence of tube diameter, moisture and diameter-definition by Geldart C fines content, Powder Technol. 235 (2013) 1038–1046, https://doi.org/10.1016/j.powtec.2012.12.002.
[40] N.I. Gelperin, V.G. Ainshtein, L.A. Korotyanskaya, Heat transfer between a fluidized bed and staggered bundles of horizontel tubes, Int. Chem. Eng. 9 (1969) 137–142.
[41] H.-J. Natusch, B. Neukirchen, R. Noack, Lokale Wärmeübergangszahlen für ein Einzelrohr und für Rohrbündel verschiedener Anordnung in Wirbelschichten, Forschungs-Gesellschaft Verfahrenstechnik e.V, Stuttgart, 1975.
[42] K.B. Schwaiger, Development of a Novel Particle Reactor/Heat-Exchanger Technology for Thermal Energy Storages, Thesis, Technische Universität Wien, 2016. https://repositum.tuwien.at/handle/20.500.12708/158429 (accessed June 11, 2025).
[43] C. Eder, G. Hofer, T. Pröll, Wall-to-bed heat transfer in bubbling fluidized bed reactors with an immersed heat exchanger and continuous particle exchange, Ind. Eng. Chem. Res. 60 (2021) 7417–7428, https://doi.org/10.1021/acs.iecr.0c06331.
[44] S.W. Kim, J.Y. Ahn, S.D. Kim, D.H. Lee, Heat transfer and bubble characteristics in a fluidized bed with immersed horizontal tube bundle, Int. J. Heat Mass Transf. 46 (2003) 399–409, https://doi.org/10.1016/S0017-9310(02)00296-X.
[45] S.W. Kim, S.D. Kim, Heat transfer characteristics in a pressurized fluidized bed of fine particles with immersed horizontal tube bundle, Int. J. Heat Mass Transf. 64 (2013) 269–277, https://doi.org/10.1016/j.ijheatmasstransfer.2013.04.045.
[46] S.E. Olsson, A.E. Almstedt, Local instantaneous and time-averaged heat transfer in a pressurized fluidized bed with horizontal tubes: influence of pressure, fluidization velocity and tube-Bank geometry, Chem. Eng. Sci. 50 (1995) 3231–3245, https://doi.org/10.1016/0009-2509(95)00150-4.
[47] J. Wiman, A.E. Almstedt, Hydrodynamics, erosion and heat transfer in a pressurized fluidized bed: influence of pressure, fluidization velocity, particle size and tube bank geometry, Chem. Eng. Sci. 52 (1997) 2677–2695, https://doi.org/10.1016/S0009-2509(97)00096-1.
[48] N.N. Greenwood, A. Earnshaw, Silicon, in: Chem. Elem, 2nd ed., Butterworth-Heinemann, Oxford, 1997, pp. 328–366, https://doi.org/10.1016/B978-0-7506-3365-9.50015-8.
[49] S. Thanheiser, M. Haider, Dispersion model for level control of bubbling fluidized beds with particle cross-flow, Chem. Eng. Res. Des. 216 (2025) 427–440, https://doi.org/10.1016/j.cherd.2025.02.038.
[50] K.G. Schmidt, M1 Heat Transfer to Finned Tubes, in: VDI Heat Atlas, 2nd ed., Springer, Berlin, Heidelberg, 2010, pp. 1271–1278, https://doi.org/10.1007/978-3-540-77877-6_94.
[51] G.A.F. Seber, C.J. Wild, Computational Methods for Nonlinear Least Squares, Nonlinear Regres., John Wiley & Sons, in, 1989, pp. 619–660, https://doi.org/10.1002/0471725315.ch14.
[52] L. Fahrmeir, T. Kneib, S. Lang, B.D. Marx, The classical linear model, in: Regression, 2nd ed, Springer, Berlin, Heidelberg, 2021, pp. 85–190, https://doi.org/10.1007/978-3-662-63882-8_3.
[53] S. Greenland, S.J. Senn, K.J. Rothman, J.B. Carlin, C. Poole, S.N. Goodman, D. G. Altman, Statistical tests, P values, confidence intervals, and power: a guide to misinterpretations, Eur. J. Epidemiol. 31 (2016) 337–350, https://doi.org/10.1007/s10654-016-0149-3.
[54] W. Wagner, H.-J. Kretzschmar, R. Span, R. Krauss, D2 Properties of Selected Important Pure Substances, in: VDI Heat Atlas, 2nd ed., Springer, Berlin, Heidelberg, 2010, pp. 153–300, https://doi.org/10.1007/978-3-540-77877-6_11.